

## Non-hydrostatic Modeling of Exchange Flows Across Complex Geometries

Mehmet Ilıcak<sup>a,\*</sup>, Tamay M. Özgökmen<sup>a</sup>, Emin Özsoy<sup>b</sup>, Paul F. Fischer<sup>c</sup>

<sup>a</sup> RSMAS/MPO, University of Miami, 4600 Rickenbacker Cswy, Miami, FL 33149, USA

<sup>b</sup> Institute of Marine Sciences, Middle East Technical University, Erdemli, Icel, Turkey

<sup>c</sup> Mathematics and Computer Science Division, Argonne National Laboratory, Argonne, IL, USA

### ARTICLE INFO

#### Article history:

Received 24 November 2008

Received in revised form 14 April 2009

Accepted 16 April 2009

Available online 3 May 2009

#### Keywords:

Exchange flows

Bosphorus strait flow

VLES

Hydraulic control

### ABSTRACT

Flows between ocean and marginal sea basins are often connected by narrow channels and shallow sills. In this study, we address the effect of lateral and vertical geometric constrictions on mixing and hydraulic control. We conduct a set of numerical experiments of the lock-exchange problem in the presence of lateral and vertical contractions. Large eddy simulations (LES) are carried out using the high-order non-hydrostatic spectral element model Nek5000. A spanwise-averaged 2D non-hydrostatic model, denoted SAM, is also employed. Comparison between 2D and 3D models are conducted on the basis of the shape of the density interface and the time evolution of the background potential energy that quantifies the cumulative effects of the stratified mixing in the system.

LES indicates that an S-shaped channel induces the highest amount of mixing possibly due to the additional shears caused by the centrifugal force. Vertical and horizontal constrictions enhance mixing by the trapping and breaking of the internal waves in between the obstacles. On the other hand, vertical and horizontal constrictions overlapping with each other restrain the rate of the exchange flow, reduce vertical shears and the mixing. The lowest mixing is encountered in a V-shaped channel. It is also found that SAM appears to be accurate in identifying the hydraulic control points due to both horizontal and vertical constrictions. A good agreement is found between SAM and inviscid two-layer theory regarding the steady-state location of the density interface. However SAM overestimates mixing with respect to LES since overturning eddies tend to merge in 2D, while they break down into smaller scales in 3D.

SAM is then further tested a realistic application to model the flow in the Bosphorus Strait. Here, the main challenges of using SAM revolved around a non-trivial reduction of 3D geometry to a 2D mapping function, and excessive diffusion with simple closures. The realism of SAM improves significantly using a comprehensive turbulence closure of Very Large Eddy Simulation, VLES.

In conclusion, exchange flows in narrow straits pose significant computational challenges due to the details of domain geometry and their impact on mixing. SAM with the VLES turbulence closure appears to be an attractive modeling tool for a first-order assessment of dynamical problems involving mixing and hydraulic effects.

© 2009 Elsevier Ltd. All rights reserved.

### 1. Introduction

Exchange flows often occur at straits or inlets connecting two basins of water with contrasting properties, found at so many localities on earth. About 30 major straits can be identified in the marginal seas of Europe alone, with almost a half of them characterized by narrows or other complex geometric features constraining the exchange. Because high current velocities are often generated at straits, and are accentuated by geometric constraints, the resulting flows are typically highly nonlinear and time-dependent on inertial to multi-annual climatic time scales. The variability on this wide range of scales often has important consequences

reflected not only locally, but also on processes in the adjacent seas.

Mixing within straits occurs via interfacial shear, eddies, either near geometric irregularities or by hydraulic adjustment. Upon exit to adjacent seas either the surface low density plumes or the bottom dense water plumes continue to dominate mixing and spreading near the exit by processes of turbulent entrainment, recirculation, meandering, shelf break cascading, and positive or negative buoyant spreading, thus largely influencing the renewal and basin-wide material cycles of adjacent basins. Often the biogeochemical interactions between adjacent basins, the seasonal migrations or spawning strategies of some fish species from these regions critically depend on these processes.

Motivated by the problem of exchange flows in narrow straits, we aim to make progress in addressing the following questions:

\* Corresponding author. Tel.: +1 (305) 421 4654.

E-mail address: [milicak@rsmas.miami.edu](mailto:milicak@rsmas.miami.edu) (M. Ilıcak).

- How do the lateral and vertical contractions affect mixing?
- Given the narrow straits, how accurate can the exchange process be captured using a 2D non-hydrostatic model?
- Can a 2D model be modified to adequately capture the effect of lateral geometric variations on the flow field?
- How sensitive is mixing on the spatial resolution and subgrid-scale mixing closures used in the 2D non-hydrostatic model?

We approach this problem by first conducting large eddy simulations, LES, of the lock-exchange problem in the presence of lateral and vertical contractions. These 3D computations are carried out using the non-hydrostatic spectral element model Nek5000 (Fischer, 1997; Fischer et al., 2000) which combines the geometrical flexibility of the finite-element method with the numerical accuracy of the spectral expansion. For LES, the dynamic Smagorinsky sub-grid scale (SGS) model (Germano et al., 1991; Porté-Agel et al., 2000; Meneveau et al., 1996) is used, in which the test filtering exploits the high-order discretization of the spectral element model. In parallel, we carry out simulations using a 2D non-hydrostatic model, which is based on the lateral averaging procedure introduced by Bourgault and Kelley (2004). The LES model not only helps quantify mixing in different geometrical settings, but also serves as the ground truth for the 2D runs. A detailed comparison is conducted on the basis of the shape of the density interface and the time evolution of the background potential energy that quantifies the cumulative effects of the stratified mixing in the system.

The non-hydrostatic 2D model is then used to model the exchange flow through the Bosphorus Strait. Despite existing studies, very few detailed studies have been made in order to compare and quantify mixing processes at straits with geometries of multiple horizontal and vertical geometrical constrictions, for example those similar to those complex features encountered at the Bosphorus. Ocean circulation models developed for either the open ocean or the coastal waters often do not have all the necessary ingredients to allow such investigations, namely non-hydrostatic dynamics and/or a suite of turbulence closures. On the other hand, while it is possible to address some of the questions posed by going to a full resolution non-hydrostatic fluid dynamical models, namely the direct numerical simulation DNS, such simulations still pose grand computational challenges, and as such, it is desirable to know how good the main mixing results can be recovered in a simpler, reduced-order or 2D model based on the lateral averaging of the governing equations in a situation where such approximations appear reasonable, such as in the Bosphorus.

The paper is organized as follows: the numerical models used in this study, the LES model and the 2D model are introduced in Section 2. The configuration of the numerical experiments is explained in Section 3. We conduct a comparison study in the basis of idealized experiments in Section 4, and then attempt a realistic application to Bosphorus in Section 5. Finally, the principal findings are summarized in Section 6.

## 2. Numerical models

### 2.1. 3D Spectral element model

The Boussinesq equations are:

$$\begin{cases} \mathbf{u}_t + \mathbf{u} \cdot \nabla \mathbf{u} + \frac{1}{\rho_0} \nabla p - \nu \nabla^2 \mathbf{u} + \frac{\rho'}{\rho_0} \mathbf{g} \mathbf{k} = 0, \\ \nabla \cdot \mathbf{u} = 0, \\ \rho'_t + \mathbf{u} \cdot \nabla \rho' - \kappa \nabla^2 \rho' = 0, \end{cases} \quad (1)$$

where  $\Delta$  is the Laplacian operator,  $\rho_0$  the constant fluid density,  $\rho'$  is the density perturbation in a fluid with density  $\rho = \rho_0 + \rho'$  such that  $\rho' \ll \rho_0$ ,  $p$  the pressure,  $\nu$  the kinematic viscosity,  $\kappa$  the molec-

ular diffusivity,  $g$  the gravitational acceleration, and  $\mathbf{k}$  the unit normal vector in the vertical direction.

The model parameters are obtained non-dimensionalizing the Boussinesq equations (1) using  $\mathbf{u} = U\mathbf{u}^*$ ,  $\mathbf{x} = H\mathbf{x}^*$ ,  $t = \frac{H}{U}t^*$ ,  $p = \rho_0 U^2 p^*$ ,  $\rho' = \Delta\rho' \rho'^*$ , where  $U$  is the characteristic speed scale of the problem, namely the initial gravity current speed,  $H$  is the domain depth away from the vertical contractions, and  $\Delta\rho'$  is the density difference between the two main water masses. Dropping “\*” for nondimensional variables, we get

$$\begin{cases} \mathbf{u}_t + \mathbf{u} \cdot \nabla \mathbf{u} + \nabla p - \frac{1}{Re} \nabla^2 \mathbf{u} + \frac{1}{Fr^2} \rho' \mathbf{k} = 0 \\ \nabla \cdot \mathbf{u} = 0 \\ \rho'_t + \mathbf{u} \cdot \nabla \rho' - \frac{1}{RePr} \nabla^2 \rho' = 0, \end{cases} \quad (2)$$

where the nondimensional parameters are the Reynolds number  $Re = UH/\nu$ , the Prandtl number  $Pr = \nu/\kappa$ , and the Froude number  $Fr = U/(NH)$  with  $N = \left(\frac{g\Delta\rho'}{\rho_0 H}\right)^{1/2}$  being the buoyancy frequency.

Equation set (2) is solved using the model Nek5000. Nek5000 is based on the spectral element method (Patera, 1984; Maday and Patera, 1989; Fischer, 1997; Deville et al., 2002), which combines the high-order accuracy of spectral methods with the geometric flexibility of traditional finite-element methods. The time advancement of the Boussinesq equations (1) is based on third-order semi-implicit operator-splitting methods (Maday et al., 1990; Fischer, 1997). Spatial discretization is based on the spectral element method, which is a high-order weighted residual technique based on compatible velocity and pressure spaces free of spurious modes. Locally, the spectral element mesh is structured, with the solution, data, and geometry expressed as sums of  $N$ th-order Lagrange polynomials on tensor-products of Gauss-Lobatto-Legendre (GLL) quadrature points. Globally, the mesh is an unstructured array of  $K$  deformed hexahedral elements and can include geometrically nonconforming elements. For problems having smooth solutions, the spectral element method achieves exponential convergence with  $N$ , despite having only  $C^0$  continuity, which is advantageous for parallelism.

For problems involving the complex interaction of stratified flows with topography, such as in many oceanic and coastal situations, Nek5000 offers the following three important advantages. The first is that the spectral element method offers a dual approach to convergence: algebraic via elemental grid refinement, and exponential via increase in the order of intra-element interpolation. The lack of numerical dissipation and excellent phase properties are critical aspects to ensure that discretized equations represent the solution of the Navier-Stokes equations. Fast convergence is essential in order to solve the problem with a minimum number of discretization points, which is especially critical in 3D problems at high Reynolds numbers. The second advantage is that Nek5000 provides the geometrical flexibility of the finite element method, which is critical in the present study. The third advantage is the scalability of the code on parallel machines. Efficient solution of the Navier-Stokes equations in complex domains depends on the availability of fast solvers for sparse linear systems. Nek5000 uses as a preconditioner the additive overlapping Schwarz method introduced by Dryja et al. (1987) and developed in the spectral element context by Fischer and Ronquist (1994), Fischer (1997), Fischer and Gottlieb (1997), Lottes and Fischer (2005). The key components of the overlapping Schwarz implementation are fast local solvers that exploit the tensor-product form and a parallel coarse-grid solver that scales to thousands of processors (Tufo and Fischer, 2001).

### 2.2. Large eddy simulation

Eq. (2) provides a full description of the fluid motion, provided that all spatial scales of motion are resolved. However, in oceanic

flows this is never the case because of the high Reynolds number,  $Re = UL/\nu$ . Using a characteristic speed scale  $U \approx 1 \text{ ms}^{-1}$ , vertical length scale  $H \approx 10^2 \text{ m}$  and kinematic viscosity  $\nu = 10^{-6} \text{ m}^2\text{s}^{-1}$ , a typical estimate can be obtained as  $Re \approx 10^8$ . Since the number of degrees of freedom in the case of homogeneous, isotropic turbulence is proportional to  $Re^{9/4}$ , we obtain  $\approx O(10^{18})$  for the number of grid points needed for DNS of coastal flow modeling.

In LES, only the turbulent coherent structures are resolved and subgrid-scale closures are used to model the effect of unresolved scales on the resolved scales of motion. The resolved scales are obtained by applying a spatial filtering to Eq. (2) as a convolution integral, viz.,  $\bar{u}_i(\mathbf{x}, t) = \int \int \int g_\delta(\mathbf{x} - \xi) u_i(\xi, t) d^3\xi$ , where  $u_i$  denotes the full velocity,  $\bar{u}$  denotes the resolvable-scale filtered velocity,  $\delta = (\Delta x \Delta y \Delta z)^{1/3}$  is the filter width as a function of model spatial resolution, and  $g_\delta$  is the filter function. The filtered non-dimensional Boussinesq equations become

$$\begin{cases} \bar{\mathbf{u}}_t + \bar{\mathbf{u}} \cdot \nabla \bar{\mathbf{u}} + \nabla \bar{p} - Re^{-1} \nabla^2 \bar{\mathbf{u}} + Fr^{-2} \bar{\rho} \mathbf{k} = -\nabla \cdot \tau, \\ \nabla \cdot \bar{\mathbf{u}} = 0, \\ \bar{\rho}_t + \bar{\mathbf{u}} \cdot \nabla \bar{\rho} - (Re Pr)^{-1} \nabla^2 \bar{\rho} = -\nabla \cdot \sigma, \end{cases} \quad (3)$$

where  $\tau = \overline{\mathbf{u}\mathbf{u}} - \bar{\mathbf{u}}\bar{\mathbf{u}}$  and  $\sigma = \overline{\mathbf{u}\rho} - \bar{\mathbf{u}}\bar{\rho}$  are the subgrid-scale (SGS) stresses exerted by the unresolved on the resolved scales on motion. In practice, a filter is not actually applied to the computational field, but it is assumed that the restriction of the computed fields to the numerical grid constitutes the filtering procedure.

Here, the dynamic Smagorinsky SGS model is used:

$$\tau = -2(c_{ds}\delta)^2 |\nabla^s \bar{\mathbf{u}}| \nabla^s \bar{\mathbf{u}}, \quad (4)$$

where  $\nabla^s \bar{\mathbf{u}} := (\nabla \bar{\mathbf{u}} + \nabla \bar{\mathbf{u}}^T)/2$  is the deformation tensor of  $\bar{\mathbf{u}}$ . The Smagorinsky constant  $c_{ds}$  is computed dynamically from (Germano et al., 1991; Porté-Agel et al., 2000; Meneveau et al., 1996):

$$c_{ds}^2 = \frac{1}{2} \frac{\langle M_{ij} L_{ij} \rangle}{\langle M_{kl} M_{kl} \rangle}. \quad (5)$$

In (5),  $\langle \cdot \rangle$  denotes spanwise-averaging,

$$M_{ij} := \tilde{\delta}^2 |\nabla^s \tilde{\mathbf{u}}| \nabla^s \tilde{\mathbf{u}}_{ij} - \delta^2 |\nabla^s \bar{\mathbf{u}}| \nabla^s \bar{u}_{ij} = \delta^2 \left( \alpha^2 |\nabla^s \tilde{\mathbf{u}}| \nabla^s \tilde{\mathbf{u}}_{ij} - |\nabla^s \bar{\mathbf{u}}| \nabla^s \bar{u}_{ij} \right) \quad (6)$$

$$L_{ij} = \tilde{u}_i \tilde{u}_j - \bar{u}_i \bar{u}_j, \quad (7)$$

where a tilde denotes filtering with a test filter of radius  $\tilde{\delta}$  and  $\alpha := \tilde{\delta}/\delta$  is the filter ratio. Defining  $\bar{M}_{ij} := M_{ij}/\delta^2$ ,  $c_{ds}$  is computed from

$$c_{ds}^2 = \frac{1}{2} \frac{\langle \bar{M}_{ij} L_{ij} \rangle}{\langle \bar{M}_{kl} \bar{M}_{kl} \rangle}, \quad (8)$$

which depends only on the ratio of filter widths  $\alpha$  and has no explicit dependence on  $\delta$ . If one constructs a test filter that projects onto half of the number of modes, then  $\alpha = 2$ . In the context of the spectral element method used here, we project from the  $N$ th-order local basis functions onto a basis of order  $\tilde{N}$ , with corresponding  $\alpha = N/\tilde{N}$ . This allows the test filter regime of  $\alpha < 2$ . In the LES computations here,  $1.18 \leq \alpha \leq 1.5$ . The main advantage of the dynamic estimation procedure with respect to a constant-coefficient implementation (typically  $0.05 \leq c_s \leq 0.17$ ) is its ability to correctly yield  $c_{ds} = 0$  in laminar regions of the flow, thereby avoiding excessive dissipation.

We have recently conducted an extensive comparison of the performance of different SGS models in the lock-exchange problem (Özgökmen et al., 2009). The SGS models included not only (4), but also approximate deconvolution (Iliescu and Fischer, 2003, 2004) and hybrid types. It was found that approximate deconvolution models improve the solution by helping preserve the detail of turbulent coherent structures on coarse meshes. But, this improve-

ment shows up in the longer term, after many travel periods along the domain. Since the integrations are limited to a single travel period here, the SGS model (4) as well as none for the density perturbation,  $\sigma = 0$ , are deemed satisfactory.

Nek5000 has been used in the numerical simulation of bottom gravity currents (Özgökmen et al., 2004a,b, 2006; Özgökmen and Fischer, 2008) and these results have been useful to refine parameterizations of gravity current mixing for an ocean general circulation model (Chang et al., 2005; Xu et al., 2006).

### 2.3. Spanwise-averaged Boussinesq model

The 2D model is based on the vorticity-streamfunction formulation, and the governing equations are derived from laterally-averaged 2D equations of primitive variables in Bourgalet and Kelley (2004). The non-dimensionalized model equations are

$$\begin{aligned} \frac{\partial \zeta}{\partial t} + \frac{1}{B} J(\psi, \zeta) + \zeta \frac{J(B, \psi)}{B^2} = & -\frac{1}{Fr^2} \left( \frac{\partial \rho'}{\partial x} \right) + \frac{1}{Re} \nabla^2 \zeta + \frac{1}{B} \frac{\partial}{\partial x} \left( \frac{B}{Re_t} \frac{\partial \zeta}{\partial x} \right) \\ & + \frac{1}{B} \frac{\partial}{\partial z} \left( \frac{B}{Re_t} \frac{\partial \zeta}{\partial z} \right), \end{aligned} \quad (9)$$

$$\begin{aligned} \frac{\partial \rho'}{\partial t} + \frac{1}{B} J(\psi, \rho') = & \frac{1}{Re Pr} \nabla^2 \rho' + \frac{1}{B} \frac{\partial}{\partial x} \left( \frac{B}{Re_t Pr_t} \frac{\partial \rho'}{\partial x} \right) \\ & + \frac{1}{B} \frac{\partial}{\partial z} \left( \frac{B}{Re_t Pr_t} \frac{\partial \rho'}{\partial z} \right), \end{aligned} \quad (10)$$

$$\nabla \cdot \left( \frac{1}{B} \nabla \psi \right) = \zeta, \quad (11)$$

where  $\psi$  is the stream function,  $\zeta$  is the vorticity, and  $B$  is the width of the domain. The Jacobian  $J(a, b) = \frac{\partial a}{\partial x} \frac{\partial b}{\partial z} - \frac{\partial b}{\partial x} \frac{\partial a}{\partial z}$  is discretized using the Arakawa (1966) scheme to conserve both energy and enstrophy. A conformal mapping is used to convert complex topography in physical coordinates  $(x, z)$  into a rectangular domain in computational coordinates  $(\xi, \eta)$ . The ensuing equations are discretized with finite differences. The Poisson Eq. (11) is solved using a multigrid solver called MUDPACK developed by Adams (1990). The vorticity equation (9) is advanced in time using Adams-Bashforth-3 method. Density transport equation (10) relies on Flux Corrected Transport Zalesak method to eliminate Gibbs oscillations (Zalesak, 1978). More details about the numerical solution of this 2D model can be found in Ilıcak et al. (2008). Here, we refer to this 2D model given in (9)–(11) as the spanwise-averaged model or SAM.

Two types of mixing closures are incorporated and tested in SAM. In the first one, the turbulent Reynolds number,  $Re_t$ , is computed from a Richardson number dependent Smagorinsky model,

$$Re_t = \left[ (C_S \delta_{2D})^2 \mathcal{F} |f(Ri)| \right]^{-1}, \quad (12)$$

where  $C_S = 0.17$  is the Smagorinsky constant and  $\delta_{2D} = \sqrt{\Delta x \Delta z}$  is the filter scale as a function of model resolution.  $\mathcal{F} = \frac{\partial U}{\partial z} + \frac{\partial W}{\partial x}$  is the nondimensional shear, where  $U = -\frac{\partial \psi}{\partial z}$  and  $W = \frac{\partial \psi}{\partial x}$ . The Richardson number  $Ri = Fr^{-2} N^2 / \left( \frac{\partial W}{\partial z} \right)^2$  is the ratio of the square of the nondimensional buoyancy frequency  $N^2 = -\frac{\partial \rho'}{\partial z}$  and vertical shear.  $f(Ri)$  is a function used in 2D lock-exchange studies by Özgökmen et al. (2007),

$$f(Ri) = \begin{cases} 1 & \text{for } Ri < 0, \\ \sqrt{1 - \frac{Ri}{Ri_c}} & \text{for } 0 \leq Ri \leq Ri_c, \\ 0 & \text{for } Ri > Ri_c, \end{cases} \quad (13)$$

where  $Ri_c = 0.25$  is the critical Richardson number. Turbulent Prandtl number,  $Pr_t$ , is taken as 1 which corresponds to the case where eddy viscosity is equal to eddy diffusivity. The closure (12) is essentially a variant of the LES approach, albeit in 2D.

We have also tested so-called Very large eddy simulation (VLES) introduced by Magagnato and Gabi (2002) and Ruprecht et al.

(2003), as it seemed to work well in a recent oceanic application (Ilıcak et al., 2008). The main idea in VLES is to use more comprehensive SGS models than in common LES, and in particular to employ second order turbulence closures, which are based on Reynolds-Averaged Navier Stokes (RANS) equations. As such, VLES can rely more on parameterization and less on resolved turbulent coherent structures. It is hoped that this will either reduce the computational demands in VLES models, or make them more appropriate for oceanic cases, in which turbulent coherent structures can be significantly underresolved. In VLES, a length scale filter,  $\delta$ , is applied to the standard  $k - \varepsilon$  closure (Ilıcak et al., 2008). The transport equations for non-dimensional turbulent kinetic energy,  $k$ , and its dissipation rate,  $\varepsilon$ , are then given by

$$\frac{\partial k}{\partial t} + \frac{1}{B} J(\psi, k) = \mathcal{P} + \mathcal{B} - \varepsilon + \frac{1}{Re} \nabla^2 k + \frac{1}{B} \frac{\partial}{\partial x} \left( \frac{B}{Re_t \sigma_k} \frac{\partial k}{\partial x} \right) + \frac{1}{B} \frac{\partial}{\partial z} \left( \frac{B}{Re_t \sigma_k} \frac{\partial k}{\partial z} \right), \quad (14)$$

$$\frac{\partial \varepsilon}{\partial t} + \frac{1}{B} J(\psi, \varepsilon) = \frac{\varepsilon}{k} [c_{\varepsilon 1} (\mathcal{P} + c_{\varepsilon 3} \mathcal{B}) - c_{\varepsilon 2} \varepsilon] + \frac{1}{Re} \nabla^2 \varepsilon + \frac{1}{B} \frac{\partial}{\partial x} \left( \frac{B}{Re_t \sigma_\varepsilon} \frac{\partial \varepsilon}{\partial x} \right) + \frac{1}{B} \frac{\partial}{\partial z} \left( \frac{B}{Re_t \sigma_\varepsilon} \frac{\partial \varepsilon}{\partial z} \right). \quad (15)$$

In equations (14) and (15),  $\mathcal{P}$  is the production term due to shear forces, and  $\mathcal{B}$  is due to buoyancy forces,

$$\mathcal{P} = \frac{1}{Re_t} \left[ \left( \frac{\partial U}{\partial z} + \frac{\partial W}{\partial x} \right)^2 + 2 \left( \frac{\partial U}{\partial x} \right)^2 + 2 \left( \frac{\partial W}{\partial z} \right)^2 \right], \quad (16)$$

$$\mathcal{B} = \frac{1}{Fr^2 Re_t Pr_t} \left( \frac{\partial \rho'}{\partial z} \right). \quad (17)$$

The coefficients used in this  $k - \varepsilon$  model are listed in Table 1. In this study, Kantha and Clayson (1994) stability functions are used to compute turbulent Prandtl number,  $Pr_t$ .

The primary difference between VLES and RANS approaches is that the VLES closure is dependent on the model resolution. This is attained by modulating the turbulent kinetic energy according the following criterion:

$$\hat{k} = \begin{cases} k & \text{if } \delta \geq \ell, \\ (\delta \varepsilon)^{2/3} & \text{if } \delta < \ell, \end{cases} \quad (18)$$

where the symbol, “ $\wedge$ ”, represents spatial filtering and  $\ell = (k^{3/2})/\varepsilon$  is the turbulent length scale. The length scale filter is computed from

$$\delta = \alpha \cdot \max \left\{ \frac{|u| \cdot \Delta t}{\sqrt[3]{\Delta x \Delta z B(x, z)}}, \right\} \quad (19)$$

where  $\alpha = 2$  is a model constant. The dissipation rate  $\varepsilon$  is not filtered but assumed to be constant for all scales in the turbulent spectrum. The filtered turbulent kinetic energy,  $\hat{k}$ , and its dissipation rate,  $\varepsilon$ , are then resubstituted into the Eqs. (14) and (15), and turbulent Reynolds number is computed from

$$Re_t \equiv \left( c_\mu \frac{\hat{k}^2}{\varepsilon} \right)^{-1}. \quad (20)$$

### 3. Configuration of the numerical experiments

The domain for the 3D computations is  $-\frac{1}{2} \leq x \leq \frac{1}{2}$ ,  $0 \leq y \leq W$  and  $0 \leq z \leq H$ , where  $L/H = 16$  and  $W/H = 2$ , so that in the non-

**Table 1**  
Coefficients used in  $k - \varepsilon$  equations (14)–(15).

$\sigma_k$	$\sigma_\varepsilon$	$c_{\varepsilon 1}$	$c_{\varepsilon 2}$	$c_{\varepsilon 3}$	$c_\mu$
1.0	1.3	1.44	1.92	-1.0	0.09

dimensionalized setting,  $-8 \leq x \leq 8$ ,  $0 \leq y \leq 2$  and  $0 \leq z \leq 1$ . At the bottom boundary, no-slip and no-flow conditions are used, while free-slip and no-flow conditions are set at all other boundaries for the velocity components. No-flux (insulation) conditions are used for the density perturbation  $\rho'$ .

Geometrical deformations of the domain is carried out as follows. In order to introduce a vertical contraction for  $x_1 \leq x \leq x_2$  (e.g., sill), the following mapping is used in the mesh generation:

$$z' = 1 - (1 - z) \left( 1 - A \sin \left( \pi \frac{x - x_1}{x_2 - x_1} \right) \right) \quad \text{for } x_1 \leq x \leq x_2, \quad (21)$$

where  $z' \rightarrow 1$  as  $z \rightarrow 1$ , so that only the bottom boundary is deformed and the top boundary remains unperturbed.

The lateral contractions for  $x_3 \leq x \leq x_4$  are introduced using:

$$y' = y - (y + 1) A \sin \left( \pi \frac{x - x_3}{x_4 - x_3} \right) \quad \text{for } x_3 \leq x \leq x_4. \quad (22)$$

Two additional shapes are used that are characteristic of many oceanic channels. First is the vertical expansion of the geometry. A V-shaped channel is obtained from:

$$y' = y - (y + 1) A (1 - z). \quad (23)$$

Second is the S-shaped curvature along the streamwise direction, which is generated using:

$$y' = y + A \cos \left( l \pi \frac{x}{x_5} \right). \quad (24)$$

The exchange problem is initialized with dense fluid on the left that is separated from the light fluid on the right by a sharp transition layer:

$$\frac{\rho'(x, y, z, 0)}{\Delta \rho'} = \begin{cases} 1 & \text{for } -8 \leq x < -(0.005 + \eta)16, \\ 100(0.005 - x - \eta) & \text{for } -(0.005 + \eta)16 \leq x < +(0.005 - \eta)16, \\ 0 & \text{for } +(0.005 - \eta)16 \leq x \leq +8. \end{cases} \quad (25)$$

The perturbation superimposed on the density interface in order to facilitate transition to 3D flows (Fig. 1a) is  $\eta = -0.02 \sin(2\pi y)$ .

The 3D experiments are conducted in seven geometrically-different settings (Table 2). First,  $A = 0$  (geom1) which corresponds to the flat reference case (Fig. 1a). Then, a sill and a constriction are superimposed at  $x = 0$  with  $A = 0.15$  (geom2, Fig. 1b) and then with an increased geometrical deformation amplitude of  $A = 0.5$  (geom3, Fig. 1c). Two constrictions at different locations are used ( $A = 0.5$ , geom4, Fig. 1d). One sill and one constriction are placed at different locations ( $A = 0.5$ , geom5, Fig. 1e). Finally, V-shaped (geom6, Fig. 1f) and S-shaped (geom7, Fig. 1g) channels are configured.

SAM is configured in a similar way, except that no boundary conditions are needed in the span-wise direction. Vertical deformations are generated by the conformal mapping of the physical coordinates  $(x, z)$  to computational coordinates, whereas lateral deformations are introduced via the width term,  $B$ . Nondimensional  $B$  is defined as its counterpart in the 3D model:

$$B(x) = \begin{cases} 1 & \text{for } -8 \leq x < x_3, \\ 1 - A \sin \left( \pi \frac{x - x_3}{x_4 - x_3} \right) & \text{for } x_3 \leq x \leq x_4, \\ 1 & \text{for } x_4 < x \leq 8, \end{cases} \quad (26)$$

where  $B = 1$  is the width of the uncontracting channel,  $A$  is the amplitude. Different cases conducted with three different geometries are shown in Fig. 2. (i)  $A = 0$ , no contraction; (ii)  $A = 0.15$ , minimum width of the channel is 0.85; and (iii)  $A = 0.5$ , minimum width of the channel is 0.5.

Model parameters are set as follows: the Froude number is taken as  $Fr = 1$  in order facilitate critical flow and subsequent

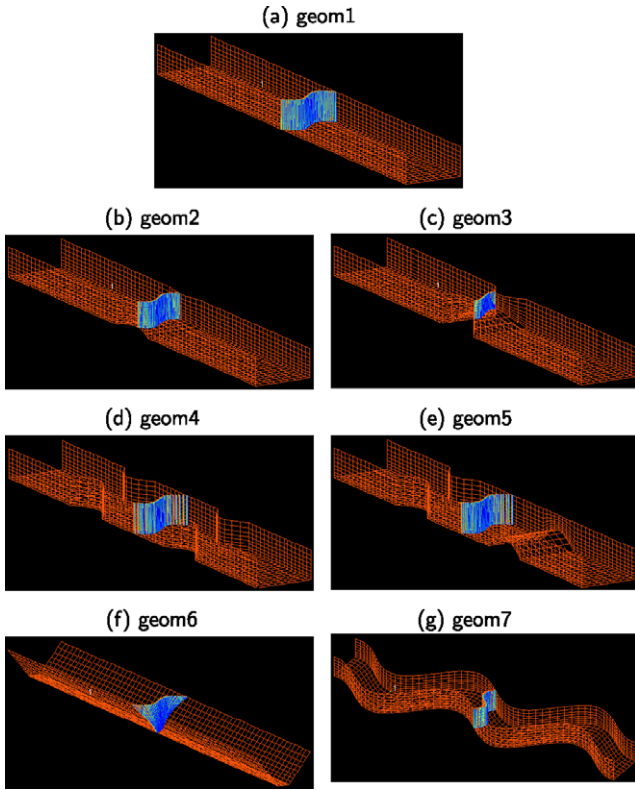


Fig. 1. Types of geometries and initializations in the 3D model.

hydraulic control and mixing. It is known that lock-exchange flows naturally tend towards critical Froude numbers (Benjamin, 1968). The Prandtl number is taken as  $Pr = 1$ . The main decision regarding the parameter selection revolves around  $Re$ . As stated above, the  $Re$  regime of the oceanic flows is unachievable using present-day computers. Our aim is to set  $Re$  high enough for the flow to show turbulent mixing, typically for  $Re > 1000$ , but not at a level where we must rely significantly on the SGS models. The SGS models have been tested using DNS at  $Re = O(10^3)$  and therefore it is not clear whether their validity extends into much higher  $Re$  regimes. Therefore, the following approach is taken. We set  $Re = 10,000$ . Then, convergence tests are carried out by changing the resolutions of DNS\*, LES, and SAM in the reference setting geom1. This allows us to settle at a resolution for all the other experiments. The convergence is evaluated on the basis of a metric that quantifies mixing in the system, which is one of our primary interests.

Table 2

Different geometries used in the 3D simulations, where  $x_1$  and  $x_2$  refer to the beginning and ending locations of the sill, while  $x_3$  and  $x_4$  refer to those for a constriction,  $x_5$  and  $l$  are the parameters of  $\mathcal{S}$ -shaped channel, and  $A$  is the amplitude of the topographic perturbation used in (21)–(24).

Geometry	$x_1$	$x_2$	$x_3$	$x_4$	$x_5$	$l$	$A$	Description
geom1	–	–	–	–	–	–	0	Flat reference case
geom2	–1	1	–1	1	–	–	0.15	Overlapping sill and constriction
geom3	–1	1	–1	1	–	–	0.50	Two constrictions
geom4	–	–	–4 and 2	–2 and 4	–	–	0.50	
geom5	–4	–2	2	4	–	–	0.50	One sill, one constriction
geom6	–	–	–	–	–	–	0.80	$\nabla$ -shaped channel
geom7	–	–	–	–	16	5	1.00	$\mathcal{S}$ -shaped channel

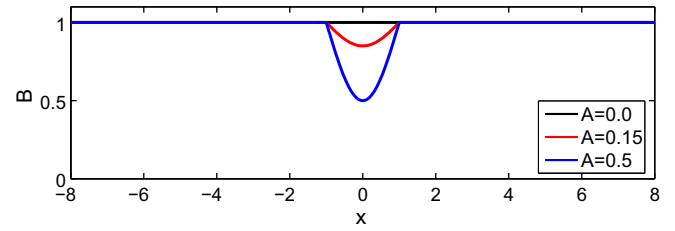


Fig. 2. Width of the contracting channel,  $B(x)$ , for different values of  $A$  from (26) used in SAM.

Mixing in an enclosed system is best quantified by changes in the background (or reference) potential energy (RPE) (Winters et al., 1995). RPE is the minimum potential energy that can be obtained through an adiabatic redistribution of the water masses, and it is computed using the probability density function approach introduced by Tseng and Ferziger (2001). In this method, the fluid is scanned every time step and the fluid parcels with a density perturbation  $\rho'$  within the range of  $[0, \Delta\rho']$  are assigned into bins between  $\rho$  and  $\rho + d\rho$ . The normalized number of control volumes in each bin gives the probability density function  $P(\rho) = V^{-1} \int_V \delta(\rho - \rho') dV$ , where  $\delta(\cdot)$  is the Dirac delta function.  $P(\rho)$  is the probability of a fluid parcel density to be in the bin of density  $\rho$ . Next, we define  $z_r(\rho')$  to be the height of fluid of density  $\rho'$  in the minimum potential energy state, which can be computed as  $z_r(\rho') = H \int_{\rho'}^{\Delta\rho'} P(\rho) d\rho$ . The background potential energy is calculated from

$$RPE = gLW \int_0^H \rho'(z_r) z_r dz_r, \quad (27)$$

by splitting the  $\rho'$  distribution into 51 bins at each time step. It is convenient to use the non-dimensional background potential energy here:

$$RPE^*(t) \equiv \frac{RPE(t) - RPE(0)}{RPE(0)}. \quad (28)$$

Fig. 3a shows  $RPE^*(t)$  in geom1 from DNS\* and LES at several resolutions, namely coarse-res LES, low-res LES, coarse-res, low-res, high-res1 and high-res2 DNS\* (Table 3). The mixing curves from high-res1 and high-res2 DNS\* are identical, ensuring that a convergence is achieved, and these curves thereby represent the truth. The differences between the curves are quite small, but coarse-res DNS\* and low-res DNS\* lead to slightly more mixing than the truth, while LES results show a nearly identical time evolution as the high-res1/high-res2 DNS\* results. Further convergence testing is conducted in the presence of geometric deformations, in setting geom2 (Fig. 3b). Here, high-res2 DNS\* (Table 3) serves as the reference curve. It is found that the result from low-res and mid-res LES is nearly identical to the reference curve from high-res2 DNS\*, while low-res DNS\* again leads to an overestimation of mixing. Similar results were found in Özgökmen et al. (2009) in that coarse-resolution DNS\* consistently tends to overestimate mixing in a lock-exchange system because instead of the high wavenumber fine structure of the instabilities, only smoothed values are captured. We find from results plotted in Fig. 3 that LES results do not show any sensitivity to spatial resolution and those from low-res LES are in good agreement with higher resolution solutions. In addition, low-res LES is 10-fold faster to run, and requires about 7-times less storage space than high-res DNS\* (Table 3). As such, all the following experiments are conducted with low-res LES.

The convergence of SAM is investigated using the resolutions listed in Table 4. Attention needs to be paid to several issues regarding a direct comparison of SAM and DNS\*. First, the 3D model has lateral boundaries, which may reduce somewhat the

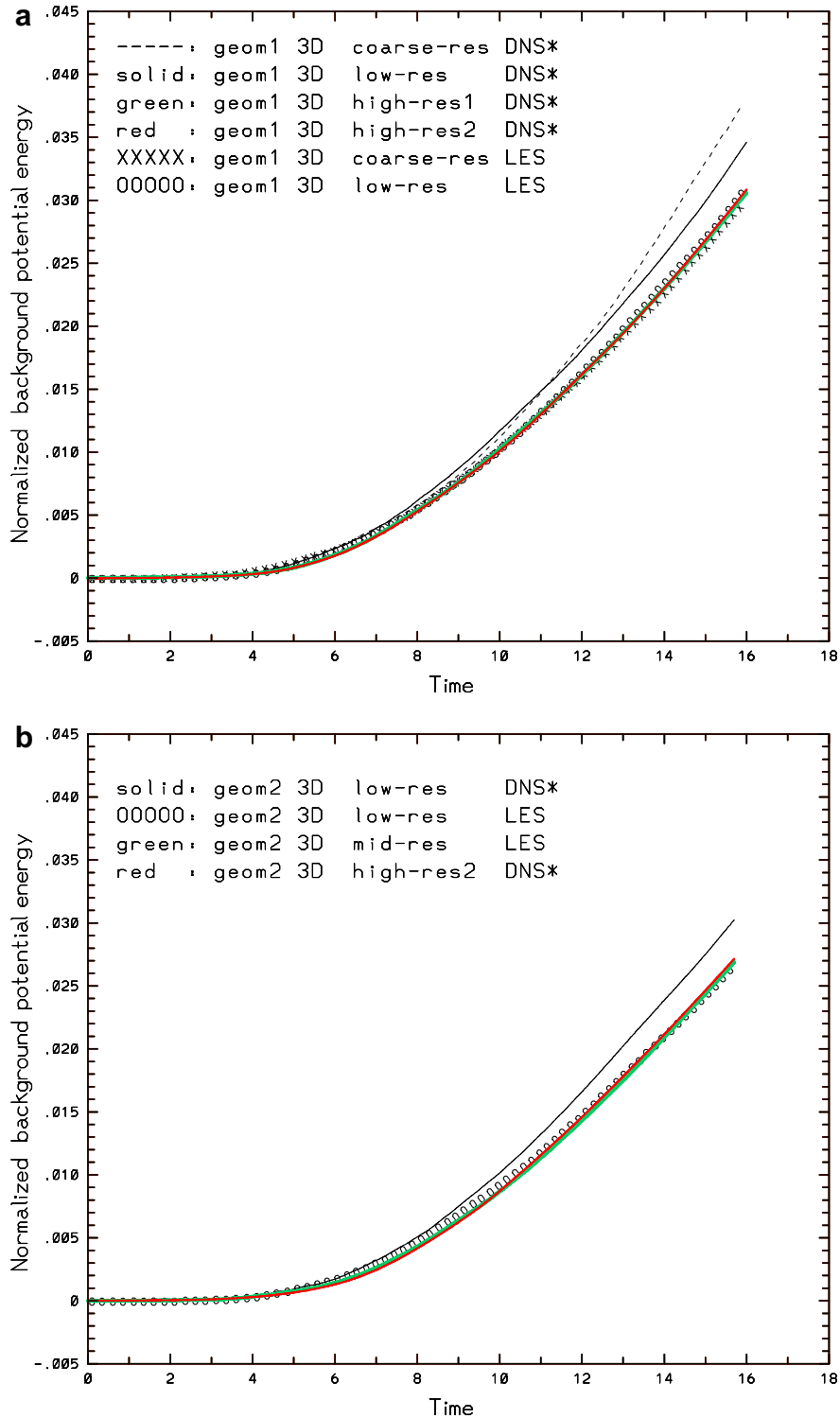


Fig. 3. Time evolution of background potential energy  $RPE^*(t)$  from DNS<sup>\*</sup> and LES with different resolutions for (a) geom1 and (b) geom2.

development of shear instabilities in the flow fields. Second, the break-down of Kelvin-Helmholtz rollers due to secondary instabilities is a dynamical mechanism that is not represented in a 2D model. Third, one would expect the convergence to be slower in a second-order finite difference model than in higher order spectral element model. Nevertheless, the comparison is necessary in order to assess the practical utility of SAM for oceanic applications, such as exchange flows in narrow straits. The  $RPE^*(t)$  curves from

SAM show a significant decrease with increasing resolution, with results from high-res SAM being very close to those from high-res DNS<sup>\*</sup>. In general, SAM shows a much wider range than DNS<sup>\*</sup> and LES results, making the selection of spatial resolution non-trivial, given also considerations of computational time. Based on Fig. 4, we decided to run the following experiments at two spatial resolutions of SAM (Table 4); with low-res because this is the 2D equivalent of the LES, and at mid-res3 because these results are quite close

**Table 3**

Table of the spatial resolutions and the typical computational cost for DNS<sup>+</sup> and LES with nek5000. The number of grid points is  $n = (K_x N + 1)(K_y N + 1)(K_z N + 1)$ , where  $N$  is the polynomial degree,  $K_x$ ,  $K_y$ , and  $K_z$  are the number of elements in  $x$ ,  $y$ ,  $z$  directions, respectively. In LES,  $\tilde{N}$  is the number of modes used for test filtering. The CPU time for  $m$  time steps to reach  $t = 16$  is listed for experiments in geom1. Wall-clock time is CPU time divided by the number of processors  $P$ . Most experiments are run on the Linux cluster based on 2.0 GHz Xeon nodes with GigE interconnect of the University of Miami's high performance computing center (<http://ccs.miami.edu/hpc/>). The symbol "∞" indicates the computations on SystemX, which can be up to 1.6 times faster than the University of Miami's cluster.

Exp	Resolution	$m$	$P$	CPU hours
DNS <sup>+</sup>	coarse-res $K_x = 64; K_y = K_z = 8; K = 4, 096; N = 6$ $n = 924, 385$	8000	16	79
DNS <sup>+</sup>	low-res $K_x = 64; K_y = K_z = 8; K = 4, 096; N = 8$ $n = 2, 167, 425$	8000	32	252
DNS <sup>+</sup>	high-res1 $K_x = 64; K_y = K_z = 8; K = 4, 096; N = 15$ $n = 14, 070, 001$	16,000	64	3,938
DNS <sup>+</sup>	high-res2 $K_x = 128; K_y = K_z = 16; K = 32, 768; N = 10$ $n = 33, 204, 801$	16,000	192	∞6144
LES	coarse-res $K_x = 64; K_y = K_z = 8; K = 4, 096; N = 6;$ $\tilde{N} = 4$ $n = 924, 385$	8000	16	128
LES	low-res $K_x = 64; K_y = K_z = 8; K = 4, 096; N = 8;$ $\tilde{N} = 6$ $n = 2, 167, 425$	8000	32	384
LES	mid-res $K_x = 64; K_y = K_z = 8; K = 4, 096; N = 13;$ $\tilde{N} = 11$ $n = 9, 183, 825$	16,000	32	3319

**Table 4**

Spatial resolutions and the typical computational cost for experiments with SAM, where  $m$  is the number of time steps to reach  $t = 16$  in geom1. The experiments are completed on a 8-processor Linux box based on 2.6 GHz dual-core Opteron chips at the University of Miami.

Exp	Resolution	$m$	$P$	CPU hours
SAM	low-res $n = 512 \times 64 = 32, 768$	16,000	2	2
SAM	mid-res1 $n = 1, 024 \times 128 = 131, 072$	16,000	2	8
SAM	mid-res2 $n = 2, 048 \times 256 = 524, 288$	16,000	2	30
SAM	mid-res3 $n = 4, 096 \times 512 = 2, 097, 152$	16,000	4	136
SAM	high-res $n = 8, 192 \times 1, 024 = 8, 388, 608$	16,000	8	560

to those from high-res but have significantly less computation time and storage requirements.

## 4. Evaluation of SAM for idealized exchange flows

### 4.1. Comparison of SAM and inviscid two-layer theory

We first compare SAM with inviscid two-layer theory by Farmer and Armi (1986). To this end, SAM is integrated in the domain setting geom3 with open boundary conditions until an approximately steady state is established. The mid-isopycnal,  $\Delta\rho/2$ , is chosen to separate the flow into two layers and to form layer Froude numbers. The lower layer thickness,  $h_2(x)$ , is taken from the bottom to the height where  $\rho' = \Delta\rho/2$ , and the upper layer thickness

$h_1(x)$  is then  $H - h_2(x)$ . Layer velocities  $u_1(x)$  and  $u_2(x)$  are computed by vertically averaging local velocities within each layer. Layer transports  $q_1(x) = u_1(x)h_1(x)B_1(x)$  and  $q_2(x) = u_2(x)h_2(x)B_2(x)$  are then computed, and the average value of  $q_r \equiv q_1/|q_2|$  is taken to characterize the flow for comparison with analytical predictions. After  $q_r$  and Fr numbers are known in the domain, non-dimensional interface height  $h_i$  can be computed from

$$h_i = \Delta H' = \frac{Fr_2^{-2/3} \left(1 + \frac{1}{2} Fr_2^2\right) - \frac{1}{2} q_r^{2/3} Fr_1^{-2/3} Fr_1^2}{q_r^{2/3} Fr_1^{-2/3} + Fr_2^{-2/3}}. \quad (29)$$

For further information about the analytical formulations, the reader is referred to Winters and Seim (2000).

In Fig. 5, we compare the prediction of  $h_i$  on the basis of the inviscid theory to  $\Delta\rho/2$  interface from SAM. The model result coincides with the inviscid theory well at the contraction and sill area. It is clearly seen that there is a hydraulic jump at  $x \approx 1.5$ . The offset between the two lines is probably mainly due to mixing in the domain. Although results between model and theory are quite similar, there are two main issues that can not be addressed in the context of this theory. The first is that the theory does not provide any information about mixing between the layers, which is usually of great interest. The second is that the flow has to be in steady-state, while oceanic flows are transient in nature. As such, we proceed to a comparison of results from SAM to those from LES.

### 4.2. Comparison of SAM and LES

Snapshots of the salinity field from simulations with low-res LES for all geom1 to geom7 are depicted in Fig. 6. The reference case geom1 has been well studied in the literature. The reader is referred to Simpson (1987) and Monaghan (2007) for comprehensive reviews on gravity currents, and to Härtel et al. (2000) and Cantero et al. (2007) for recent numerical simulations of the lock-exchange problem. Next, we summarize the main features. Once the initial interface starts tilting, two counter-propagating gravity currents are generated. The leading edges of the gravity currents propagating along the upper and lower boundaries differ because of the boundary conditions. In the presence of no-slip boundary conditions (bottom gravity current), the flow along the leading edge of the current is composed of a complex pattern of so-called lobes and clefts that are highly unsteady and well-known features from laboratory experiments tracing back to the work of Simpson (1972). It was put forth that a gravitational rise of the thin layer of light fluid that the gravity current overruns is responsible for the breakdown of the flow at the leading edge. Härtel et al. (2000) show that the instability associated with the unstable stratification prevailing at the leading edge between the nose and stagnation point of the front could also account for this behavior. In contrast, the upper gravity current traveling along a free-slip boundary does not experience such instabilities and arrives at the side boundary somewhat faster than the bottom gravity current (Fig. 6a). The shear along the interface between the two gravity currents leads to instabilities. The initial instability is in the form of 2D Kelvin-Helmholtz (KH) rolls, which constitute the usual first step toward the onset of more complex evolution of the density field. The initial 2D KH rolls are susceptible to secondary convective instability (Klaassen and Peltier, 1989, 1991), in which the stream-wise vortices stretch and tilt the span-wise vorticity concentrated in KH rolls. Consequently, KH rolls cannot sustain their lateral coherence and break down (e.g., Fritts et al. (1998), Andreassen et al. (1998)). The spanwise instability of KH rolls leads to increasingly complex turbulent interactions and smaller overturning scales; a manifestation of forward energy cascade in 3D flows. On the other hand, KH rolls tend to merge by pairing in

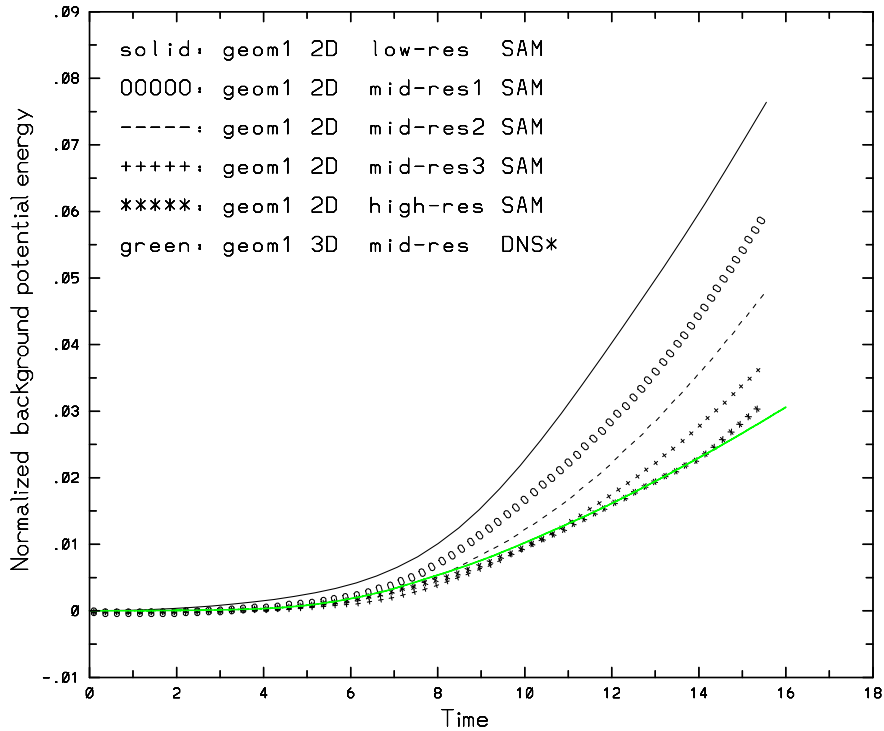


Fig. 4. Time evolution of background potential energy  $RPE^*(t)$  from SAM with different resolutions and high-res DNS\* for geom1.

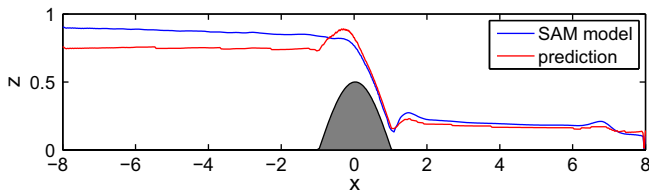


Fig. 5. Comparison of  $h_i$  from inviscid, two layer theory (29) and  $\Delta\rho/2$  from a steady-state solution of SAM for geom3.

2D dynamics (Corcos and Sherman, 1984), which is an indication of the inverse energy cascade from small to larger scales. This difference is likely to lead to a difference of amount of mixing between 2D and 3D simulations.

In order to compare qualitatively the results from low-res LES to those from SAM, spanwise-averaged density perturbation field is plotted in Fig. 7 with respect to those from low-res and mid-res3 SAM at the same times. Comparison of Fig. 7a–c shows that the density interface in SAM appears to be thicker than that in LES and is characterized by pairing KH rolls, as anticipated. The frontal positions of the gravity currents are in good agreement with one another. The lower resolution SAM experiments appear to be more diffusive than the higher resolution case, which may affect mixing.

When the domain configuration is changed to geom2, the impact is clearly visible in the flow field in the form of a hydraulic control region centered at  $x = 0$  (Figs. 6b and 7d). This results in a reduction of the thickness of the top and bottom gravity currents, and therefore a slower propagation speed so that the upper front arrives at the left boundary at  $t = 16.6$  as opposed to  $t = 16.2$  in the reference case. Hydraulic control region is less defined in SAM due to the presence of large overturning eddies, nevertheless the effect of the geometric deformation clearly changes the gravity currents propagating along both directions (Fig. 7e and f). The effect is quite significant for geom3, which leads to much thinner

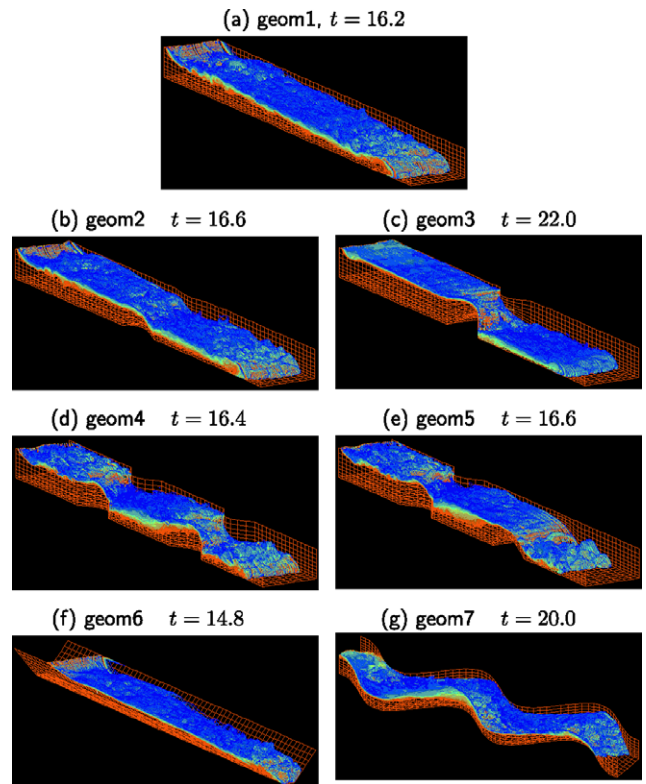


Fig. 6. Density perturbation fields at the end of experiments with low-res LES.

and slower gravity currents in both LES and SAM (Figs. 6c and 7g–i).

The hydraulic control regions created by the two constrictions (geom4) are clearly visible in LES (Figs. 6d and 8a). There is also enhanced mixing in between the two constrictions, which appears to

be induced by breaking internal waves associated with flows that do not pass through the middle part of the domain, but get reflected from the constrictions. The enhanced mixing in the region between the two constrictions appears to be greater in SAM as to obscure somewhat the hydraulic control points (Fig. 8b and c). But they are essentially in agreement with LES, which is a confirmation that spanwise-averaged formulation (9)–(11) has an effect on the flow field. Similar results are obtained for geom5 (Figs. 6e and 8d–f).

The narrowing cross section in the V-shaped channel (geom6) acts to cause a faster propagating gravity current in the bottom than near the surface (Fig. 6f). This effect is fairly accurately reproduced in SAM and the positions of the leading edges of the gravity currents are in good agreement with that from LES (Fig. 8g–i). As in all the previous cases, the vertical scale of the interfacial layer in SAM appears to be greater than that in LES due to the inability of KH rolls to break down into small-scale turbulence via lateral vortex stretching and secondary instabilities.

Finally, the snapshot of the density perturbation distribution from S-shaped channel (geom7) with LES is shown in Fig. 6g. This is an example the dynamics of which cannot be represented in a 2D model, and therefore it is of interest to know whether there is a significant difference in mixing with respect to the reference case geom1.

Several quantitative measures are used to compare SAM and LES simulations. First, the propagation speed,  $U_F(t) = dX_F/dt$ , where  $X_F$  is the position of the nose of the bottom gravity current, is computed. The propagation speed of (non-rotating) gravity currents is a good first indicator of mixing, as it was found on the basis of laboratory experiments that an increase in gravitational force from the greater slope angle is compensated by buoyancy gain from increased entrainment so that  $U_F(t)$  remains approximately constant over gentle slopes (Britter and Linden, 1980). On the basis of Figs. 7 and 8, three cases are selected to compare LES and SAM. First geom1 as the flat reference case, then geom6 to quantify the difference due to the span-wise narrowing geometry on the

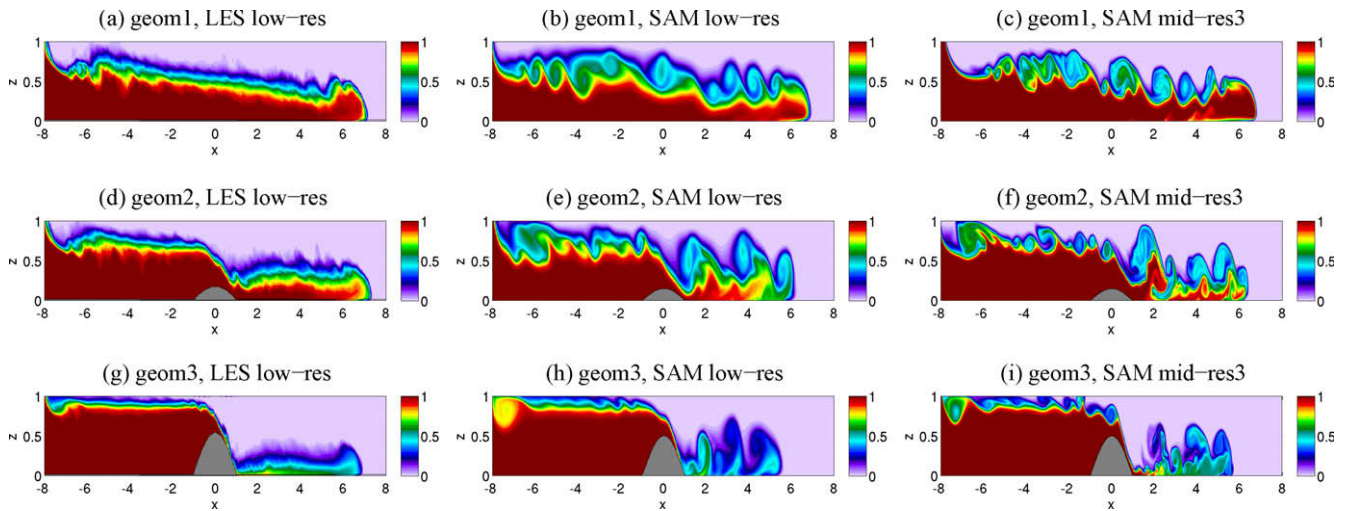


Fig. 7. Comparison of spanwise-averaged density perturbation fields from low-res LES to those low-res and mid-res3 SAM from  $RPE^*(t)$  from SAM for geom1 to geom3 at the selected times shown in Fig. 5a–c.

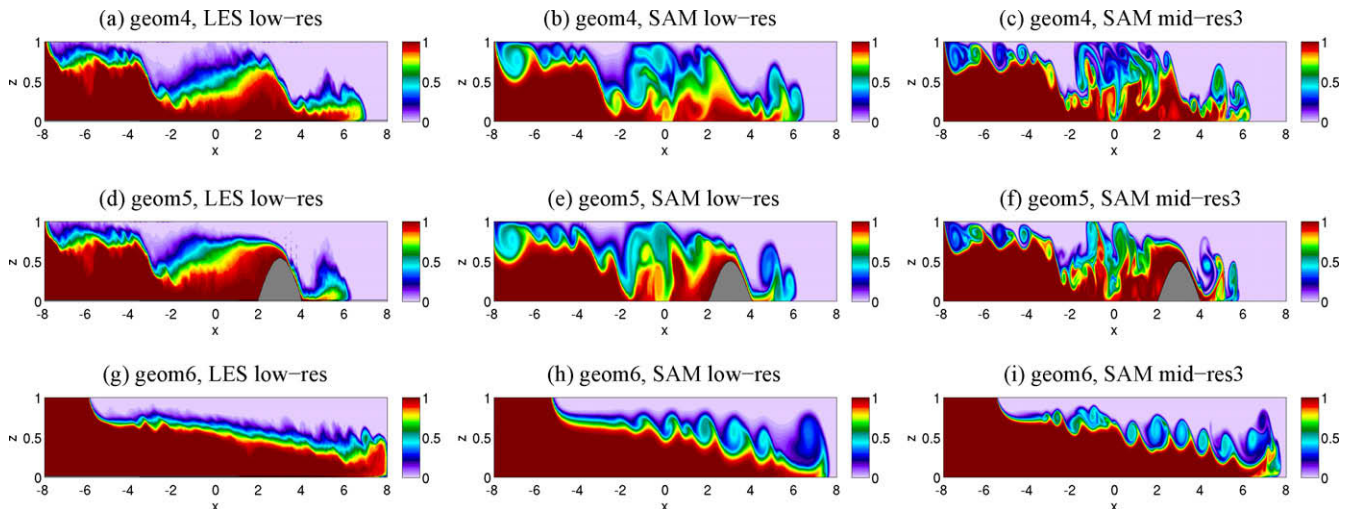
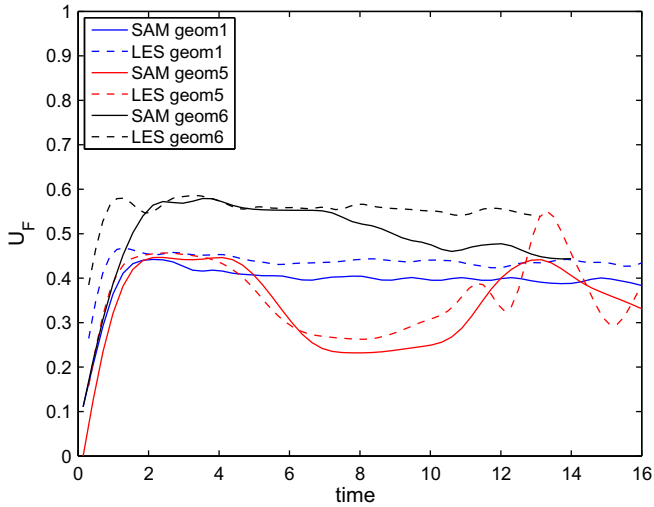


Fig. 8. Comparison of spanwise-averaged density perturbation fields from low-res LES to those low-res and mid-res3 SAM from  $RPE^*(t)$  from SAM for geom4 to geom6 at the selected times shown in Fig. 5d–f.



**Fig. 9.** The propagation speed of bottom gravity currents  $U_F(t)$  from both LES and SAM for geom1, geom5 and geom6.

propagation speed, and finally geom5 to see the effect of the sill downstream and constriction upstream on the bottom gravity current speeds. The comparison of  $U_F(t)$  is shown in Fig. 9. The bottom gravity currents from both LES and SAM attain and maintain a constant propagation speed for geom1, but  $U_F(t)$  of LES is about 10% larger than that of SAM, which is an indication of buoyancy gain due to higher mixing in SAM. The propagation speeds are larger for geom6 in comparison to geom1 and match well between SAM and LES until about  $t \approx 8$ . This agreement can be explained on the basis of little mixing during this initial phase (see Fig. 13e in the following). But then  $U_F(t)$  of SAM starts to decrease, once the large overturning eddies appear (Fig. 8g vs i). At the end of the integration, the bottom gravity current from SAM is about 15% slower than that from LES. Finally, the comparison of  $U_F(t)$  for geom5 shows that the change in the propagation speed due to the encounter with the sill is well captured in SAM.  $U_F(t)$  from LES exhibits rather large fluctuations past the sill as so-called lobe and cleft instability of the nose (Härtel et al., 2000) seems to be enhanced. This instability affects the span-wise averaging of  $X_F$  (thus  $U_F$ ) in LES (whereas it is not possible in SAM).

As a second measure to compare SAM and LES simulations, the differences of density perturbation fields shown in Figs. 7 and 8 are computed. Fig. 10 shows  $[\rho'_{LES}(t=16.2) - \rho'_{SAM}(t=16.2)]^2$  for geom1. The primary differences involve the scale of the overturning eddies, as well as the phase differences arising from the frontal propagation, as discussed above. The area-averaged rms differences between the density fields from SAM and LES are tabulated in Table 5. One of the short comings of this measure is that the phase errors from the frontal positions can be significant.

Third, we compare the time evolution of normalized potential energy  $PE(t)/PE(0)$  in Fig. 11 for the three selected cases of geom1,

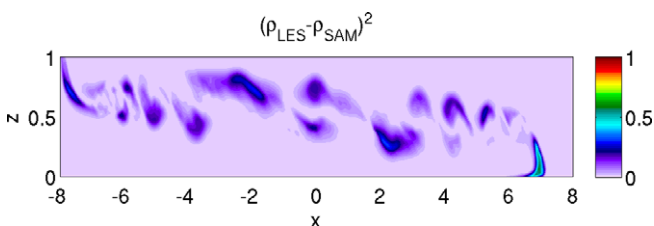


**Fig. 10.** The difference in density perturbation fields  $[\rho'_{LES}(t=16.2) - \rho'_{SAM}(t=16.2)]^2$  for geom1.

geom5 and geom6. Towards the end of the integrations, we get a difference of 3% for geom1, 1.5% for geom5 and 10% for geom6.

A precise measure of mixing is given by the background potential energy, which is of great interest and computed next. The time evolutions of the background potential energy  $RPE^*(t)$  from low-res LES are shown in Fig. 12a, which demonstrates significant differences in mixing in between different domain geometries. In particular,  $\mathcal{S}$ -shaped channel geom7 leads to the highest and geom3 to the lowest levels of mixing. Overall, the overlapping sill and constriction configurations (geom2 and geom3), and  $\nabla$ -shaped channel (geom6) act to reduce the mixing with respect to the reference case geom1. In the former, this takes place by a reduction of volume transport across the obstacle. In cases of offset obstacles (geom4 and geom5), and  $\mathcal{S}$ -shaped channel (geom7), there is a significantly higher mixing by the time one of the gravity current reaches the end of the domain.

The relative proportions of mixing in different geometries is reproduced in mid-res3 SAM in reasonable agreement with low-res LES (Fig. 12b). In other words, geom4 and geom5 lead to more mixing than geom1, while geom3 and geom6 result in less mixing. Only in the case of geom2, the result is opposite of that in LES, which could be related to large overturns seen in SAM (Fig. 7f). Overall, mid-res3 SAM tends to overestimate mixing with respect to low-res LES by a factor of 1.27 to 1.97 (Table 6).

For computational efficiency, mixing characteristics from low-res SAM are of interest. A comparison of the  $RPE^*(t)$  curves from low-res SAM, mid-res3 SAM and low-res LES for different domain geometries are depicted in Fig. 13 (Fig. 4 for geom1). It appears that mixing in low-res SAM is consistently and significantly overestimated with

**Table 5**

The rms errors between the density perturbations fields from LES and SAM for snapshots shown in Figs. 7 and 8.

Geometry	Error (%)
geom1	15.13
geom2	19.69
geom3	13.99
geom4	15.75
geom5	15.98
geom6	15.65

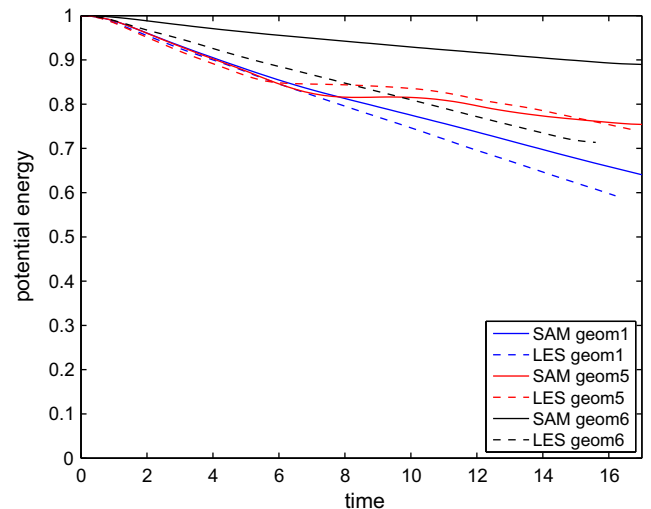


**Fig. 11.** The time evolutions of normalized potential energy  $PE(t)/PE(0)$  from both LES and SAM for geom1, geom5 and geom6.

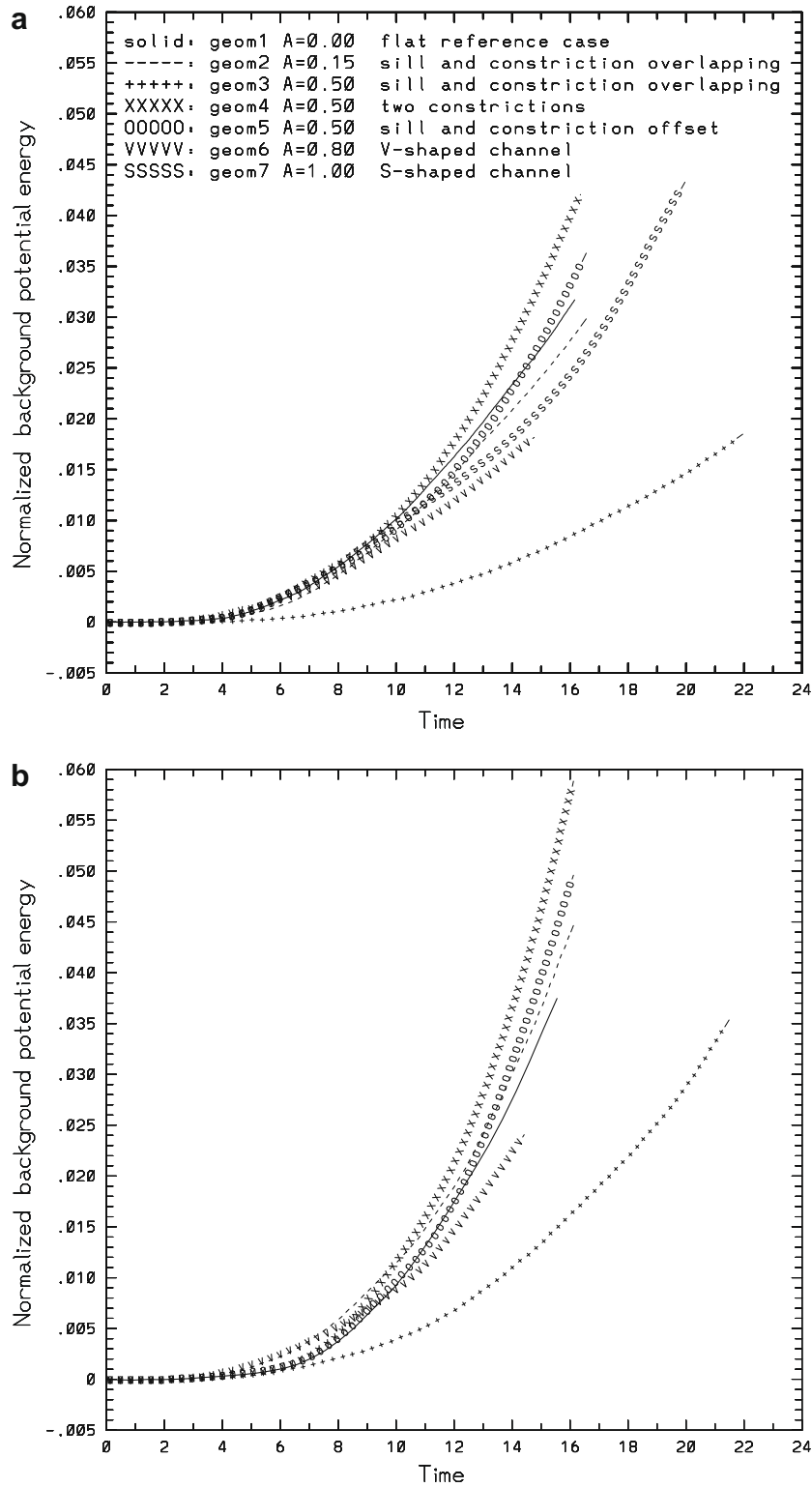


Fig. 12. Time evolution of the background potential energy  $RPE^*(t)$  for all geometrically-different cases from (a) low-res LES and (b) mid-res3 SAM.

respect to both mid-res3 SAM and low-res LES, and as such, it cannot be considered very accurate.

In conclusion, we find that SAM appears to be accurate in identifying the hydraulic control regions due to both vertical and horizontal constrictions, and also provides useful indications of the mixing in domains with complex geometries, provided high spatial resolutions are employed.

### 5. Application of SAM to Bosphorus Strait

It is of great interest to explore the applicability of SAM in a realistic oceanographic problem. To this end, we chose an important component of the the Turkish Strait System (TSS). TSS is a complex domain formed by the small internal domain of the Marmara Sea coupled with the Straits of Bosphorus and Dardanelles, an

**Table 6**

Final values of the background potential energy  $RPE^*$  at the end of the experiments for all domain geometries from low-res LES and mid-res3 SAM. The values are sorted from smallest to largest values of LES results.

Geometry	Time	$RPE^* \times 100$ low-res LES	$RPE^* \times 100$ mid-res3 SAM	$RPE^*(SAM)/RPE^*(LES)$
geom6	14.8	1.83	2.53	1.38
geom3	22.0	1.86	3.68	1.97
geom2	16.6	3.00	4.67	1.56
geom1	16.2	3.19	4.05	1.27
geom5	16.6	3.65	5.21	1.43
geom4	16.4	4.23	6.24	1.48
geom7	20.0	4.34	–	–

elongated and tortuous waterway between the European and Asian continents controlling the exchange and mixing between the Mediterranean (Aegean) and Black Sea waters, destined to determine their contrasting physical, chemical and biological properties (Fig. 14a). The TSS has been extensively studied to date. For further information the reader is referred to Ünlüata et al. (1990), Latif et al. (1991), Oğuz and Sur (1989), Oğuz (2005), Oğuz et al. (1990), Özsoy et al. (1995a,b, 1996, 1998, 2001), Özsoy and Ünlüata (1997, 1998), Polat and Tuğrul (1995), Gregg et al. (1999), Gregg and Özsoy (1999, 2002).

Two-layer stratified flow through the Bosphorus Strait is basically driven by the density difference between the Black and the Aegean Seas. In addition to density differences between basins, remote atmospheric forcing, water budgets and steric volume changes of the adjacent basins as well as the local interactions within the TSS exert dynamical forces on the system. The location of the Turkish Straits System, of which the Bosphorus is the most restrictive member, is shown in Fig. 14a and b.

The Bosphorus Strait operates in the full range of weak to strong forcing. Hydraulic controls associated with geometric features of the strait constitute a unique example of the maximal exchange regime that requires a balance with at least two critical sections, a sill and contraction with ideal configuration in the case of the Bosphorus, as foreseen by the cardinal work of Farmer and Armi (1986). Blocking of the flows in either layer occurs during extreme events corresponding to varying barotropic transports. Short-term, transient responses to meteorological events are frequently observed.

The bathymetric data used in this study (Fig. 14c) has been made available by the Turkish Navy Office of Navigation, Hydrography and Oceanography, based on the work of Gökaşan et al. (2005). Because the Bosphorus geometry is extremely complex, a simplified method was used to estimate  $B(x, z)$ . The depth and width data were computed with reference to the deepest point on the thalweg. However, in order to avoid excessive channel curvature displayed by the thalweg, width and depth data were collected on channel cross sections perpendicular to a stretched length-wise coordinate shown above. A maximum width value of 50 m was added to the width at the deepest point of each section, decreasing linearly to zero at the surface, to avoid having zero width at the bottom. This also helped reduce some noise in the determination of  $B(x, z)$ . The function  $B(x, z)$  referenced to the coordinates in Fig. 14b is shown in Fig. 14c.

An analysis based on the most detailed lengthwise sampling of salinity along the Bosphorus to date has been given in Özsoy et al. (2001). The data from the 1994 cruise of the R/V BİLİM is plotted in Fig. 15, projecting the data into the same coordinates as in Fig. 14b and c. The potential density,  $\rho$  is non-dimensionalized using the minimum ( $\rho_{\min} = 1010.39 \text{ kgm}^{-3}$ ) and the maximum ( $\rho_{\max} = 1029.24 \text{ kgm}^{-3}$ ) values as  $\bar{\rho} = (\rho - \rho_{\min}) / (\rho_{\max} - \rho_{\min})$  to conduct a model-data comparison. From these observations, one of the

most pronounced features is the hydraulic jump just after the sill around  $x = 12 \text{ km}$ , where at first isopycnals drop down then raise up again and some mixing is evident. This location also coincides with the maximum contraction point in the strait. Therefore, both geometric effects due to both the sill and contraction are likely to be important in the density structure. Another possible control point is located at  $x = 40 \text{ km}$ . Finally, the exchange flow from these observations is characterized by nearly a two-layer structure separated by a thin mixing layer.

The model is initialized as a lock-exchange problem, centered at  $x = 22.5 \text{ km}$ , where dense fluid is on the left representing the saline water originating from the Marmara Sea and light fluid is on the right representing the fresh water entering from the Black Sea (Fig. 16). The domain is 45.3 km long and has a maximum depth of 83.4 m. There are 8192 grid points used in  $x$ -direction and 64 points in  $z$ -direction ( $\Delta x \approx 5.5 \text{ m}$  and  $\Delta z \approx 1.3 \text{ m}$ ). Free-slip boundary condition is applied for the top boundary. For the bottom boundary, the Froude number  $Fr = U / \sqrt{g'h}$  is estimated using  $U \approx 1 \text{ ms}^{-1}$ ,  $g' = g \Delta \rho / \rho_0 \approx 0.18 \text{ m}^2 \text{ s}^{-1}$ ,  $h \approx 25 \text{ m}$ , and the Froude number is taken as  $Fr = 0.5$ .  $Pr$  number is set to 1 as in all the experiments above.

A set of computations consisting of five experiments is conducted. The influence of the details of the bottom boundary conditions on overflows is well known (see for instance Fig. 5 of Ilıcak et al. (2008)). Noting that this is a large-scale application, and one cannot maintain a well-resolved bottom boundary layer, we experiment with several formulations. First, the bottom boundary condition is changed from no-slip to a stress formulation with a drag coefficient of  $C_d = 2 \times 10^{-3}$ . Then, a wall damping function is used in order to alleviate the over-dissipative behavior of the constant Smagorinsky coefficient, similar to what is done in other applications (Mason, 1989; Mason and Thomson, 1992). In particular, we employ so-called van Driest damping (denoted VDD) where  $C_s$  is modified according to

$$C_{s(\text{VDD})} = C_s \left[ 1 - \exp\left(-\frac{z^+}{A}\right) \right], \quad (30)$$

where  $C_s = 0.17$ ,  $A = 25$  is the van Driest constant (Van Driest, 1956) and  $z^+$  is the non-dimensional distance from the bottom

$$z^+ = \frac{u_\tau z}{\nu}, \quad (31)$$

and  $u_\tau$  is the wall shear velocity. VDD is tested with both bottom drag and no-slip boundary condition. We set  $Re = 10^4$  in these three experiments in order to make a continuous transition from model to model comparison studies from Section 4. But, it is noted that the effective  $Re$  for the Bosphorus Strait is about  $Re = Uh/\nu \approx 25 \times 10^6$ , which is of course beyond our present computational capabilities. Nevertheless, it is important to know what types of changes occur in the simulated fields when  $Re$  is increased beyond  $10^4$ . Therefore, a fourth simulation is conducted by setting  $Re = 10^5$ . Finally, we experiment with the VLES closure introduced in Section 2.3. The typical computational cost of these experiments is listed in Table 7.

The distribution of the density perturbation from the first experiment is shown in Fig. 17a. The density field reaches nearly a steady state after non-dimensional time of 421, when the light water reaches the Marmara Sea ( $x \leq 8 \text{ km}$ ),  $B$  becomes quite large and propagation of the density front slows down significantly. The same behavior occurs when the dense water reaches the Black Sea ( $x \geq 37 \text{ km}$ ). Overall, the model shows a pronounced change in thickness across the first sill/contraction region at  $12 \leq x \leq 18 \text{ km}$ , and another at  $x = 38 \text{ km}$ .

There are essentially two major differences from the observations seen in Fig. 15. The model shows far more structure than the observations and results in a significantly more mixing, namely

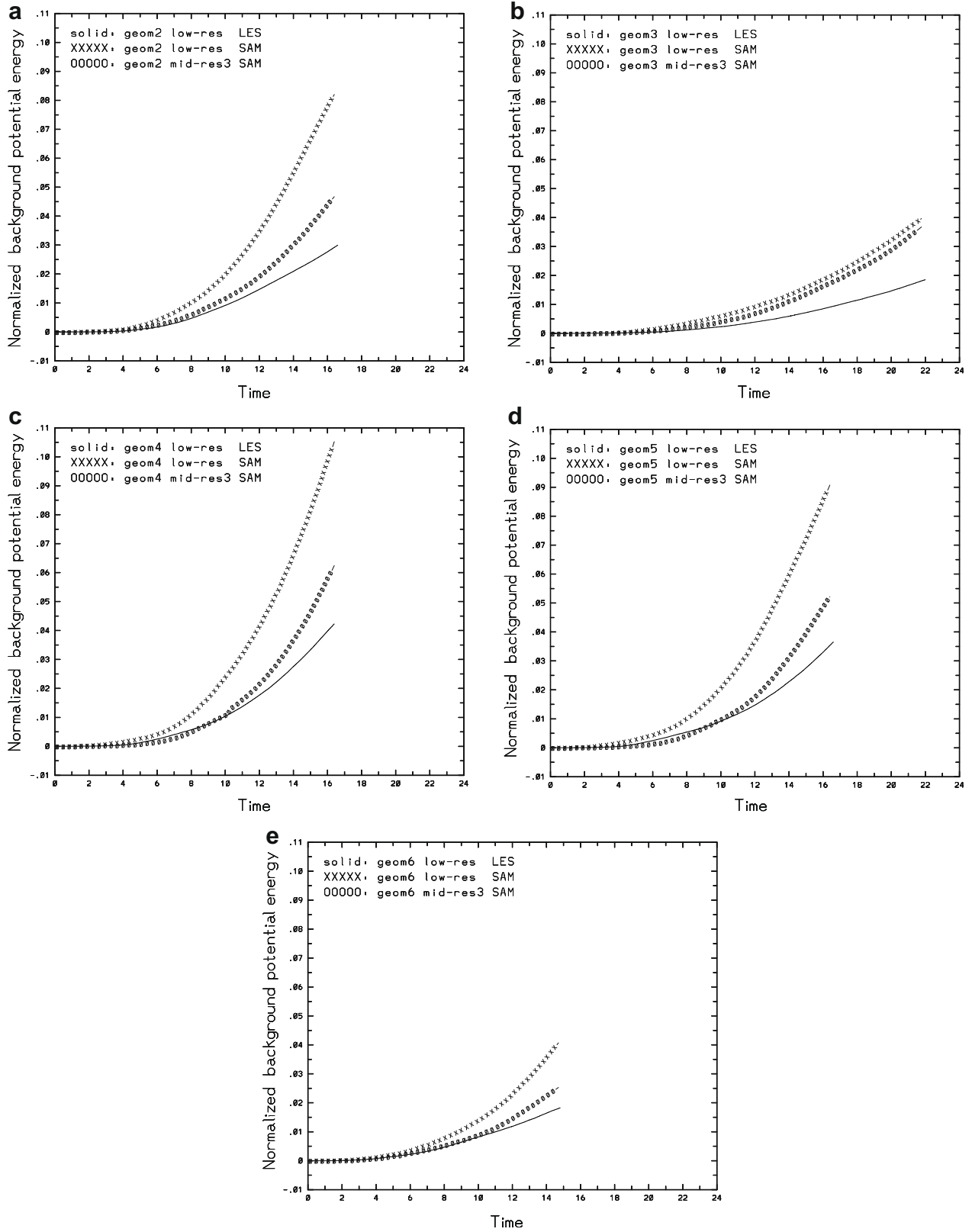


**Fig. 13.** Time evolution of background potential energy from low-res LES (solid lines), low-res SAM (lines with “X”), mid-res3 SAM (lines with “O”) for (a) geom2 to (e) geom6.

the water masses originating from the Black Sea do not reach the Marmara Sea and vice versa.

In an attempt to address these issues, VDD is added to cases with both bottom drag and no-slip boundary condition. But, as

shown in Fig. 17b and c respectively, there is no significant change, which indicates that the bulk of the excessive mixing is taking place by the interfacial shears and bottom treatment is of secondary importance. Then,  $Re$  is increased to  $10^5$  (Fig. 17d), which

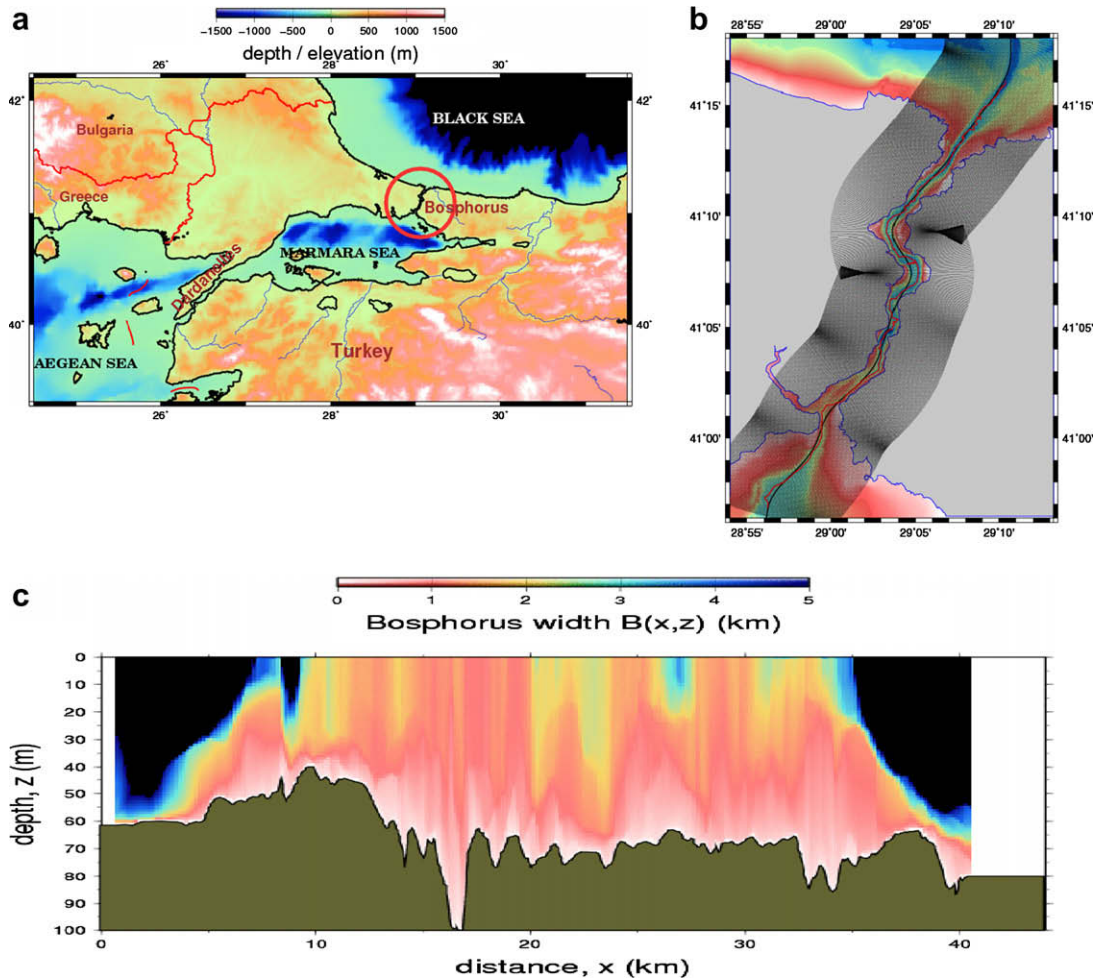


**Fig. 14.** (a) Location map for the Turkish Straits System, connecting the Black and the Mediterranean Seas via Dardanelles Strait, Marmara Sea and Bosphorus Strait. (b) The bottom topography of the Bosphorus Strait and schematics used for estimation of the width function  $B(x, z)$ . The red line is the thalweg, connecting the deepest points along the strait. Lengthwise distance,  $x$ , is referenced to the stretched black line.  $B$  is calculated at a total of 901 perpendicular sections in the shaded region. (c) The resulting  $B(x, z)$ . (For interpretation of the references to color in this figure legend, the reader is referred to the web version of this paper.)

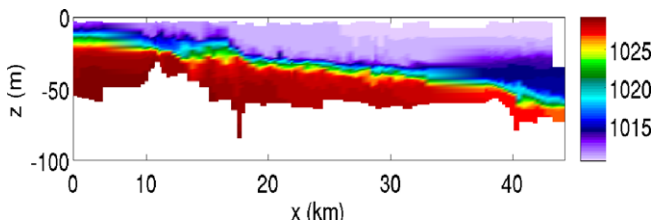


**Fig. 15.** Distribution of potential density from observations by Özsoy et al. (2001).

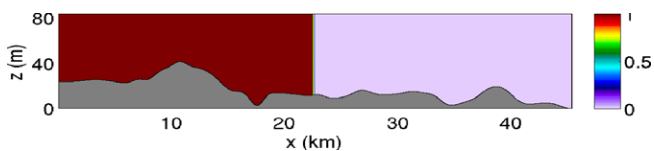


**Fig. 16.** Density perturbation at the initial state of SAM.

appears to result in a somewhat better preservation of the layer density structure than the lower  $Re$  case. Finally, the VLES closure is tested in order to explore whether it can make a difference

regarding the performance of SAM, and it is seen to lead to a significant improvement (Fig. 17e). In particular, the dense bottom water mass is much better preserved through the Bosphorus.

The discrepancy of the SAM results from the observations is likely to be related to four reasons. The first is the excessive mixing taking place in the 2D model because of lacking instabilities related to span-wise vortex stretching. Second is the generic problem of being confined to a significantly lower  $Re$  regime than the oceanic flows, which results in excessive diffusive mixing throughout the simulation period. The third is that the observations along the strait do not reflect span-wise averaged quantities but point-wise measurements so that it is not a comparison of identical quantities. Finally, is the reduction of really complex 3D geometry to 2D via the  $B$  function, for which there is not a unique solution.

In the intermediate region of  $20 \leq x \leq 35$  km, where the bottom topography is relatively flat, the density structure from all experiments appear to be correlated with the structure of  $B$

**Table 7**  
Computational cost of SAM in the applications to Bosphorus Strait.

Exp	Resolution	$m$	$P$	CPU hours
SAM with SGS (12)	$n = 8192 \times 64 = 524,288$	400,000	8	440
SAM with VLES	$n = 8192 \times 64 = 524,288$	400,000	8	768

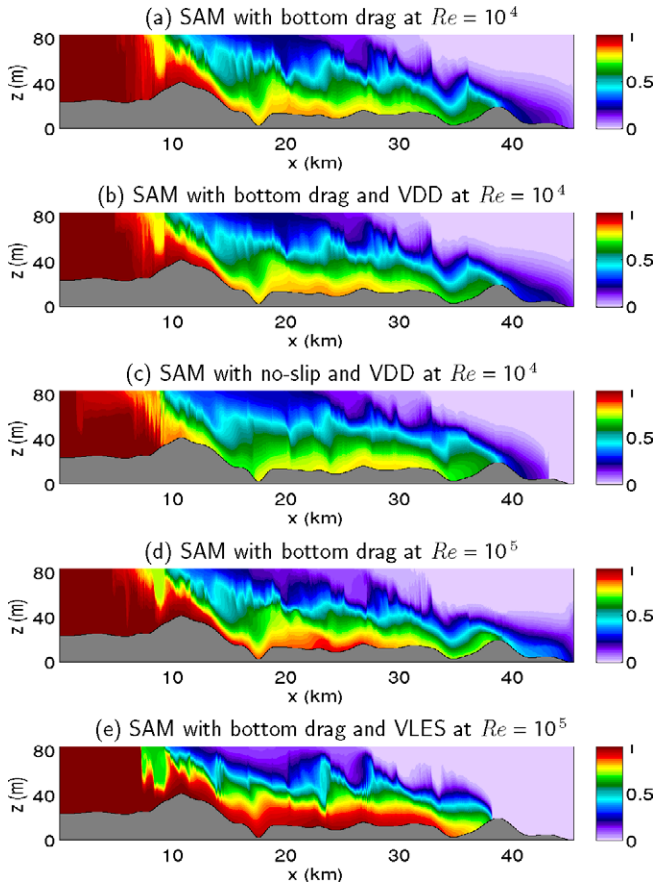


Fig. 17. Density perturbation at the final state of SAM.

(Fig. 14c). To investigate this issue in more detail, power spectra of the  $B$  function and density perturbation,  $\rho$ , are computed over the domain region with relatively flat bottom, namely for  $20 \leq x \leq 35$  km. We take 30 horizontal sections of  $B$  and  $\rho$  between  $z = 20$  m and  $z = 50$  m at every 1 m. Power spectra are computed at each section. Every power spectrum is divided by its variance, and then the mean is computed to get one profile for  $|B^2|$  and  $|\rho^2|$ . Fig. 18 shows that the power spectra of  $B$  and  $\rho$

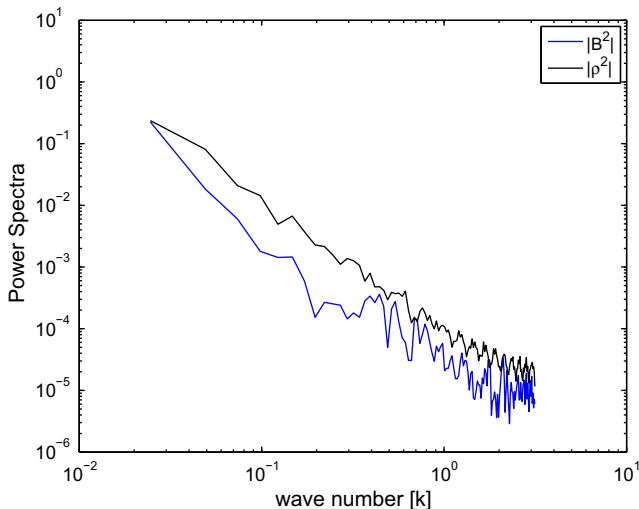


Fig. 18. Power spectra of density perturbation,  $\rho$ , and  $B$  for  $20 \leq x \leq 35$ , where the bottom topography is relatively flat.

share peaks at many wavenumbers, indicating a high correlation of their structure. In principle, the sensitivity of the solution to different realizations of the  $B$  function can be investigated. But, in essence a complete solution to this issue is only possible through the use of a fully 3D numerical model.

## 6. Summary and conclusions

In light of the importance of exchange flows in narrow straits around the world oceans, a numerical study is conducted with emphasis on the impact of domain geometry on mixing. Also, the feasibility and accuracy of a spanwise-averaged model, denoted SAM, is explored for exchange flows. This model is based on the approach introduced by Bourgault and Kelley (2004). The main motivation for testing a 2D model is the potential for significant computational gain and general simplicity with respect to a 3D model. Despite this major simplification in the equations of motion, SAM is non-hydrostatic, and also admits complex turbulence closures. As such, it is not known a-priori how well SAM will perform in the context of exchange flows, which can be computationally challenging for hydrostatic ocean models because of the large vertical velocities or small-scale mixing involved.

The study is conducted in two stages. First, we focus on a set of idealized cases in a domain with non-dimensional lengths of  $16 \times 1 \times 2$  in the horizontal, vertical and lateral directions, respectively. A set of seven cases are considered, in which geometric deformations are introduced that are generically observed in straits, namely lateral and vertical constrictions,  $\nabla$ - and  $\mathcal{S}$ -shaped channels. For these idealized cases, the ground truth is inferred from LES using a high-order spectral element model Nek5000. Non-dimensional parameters are set to  $Re = 10^4$ ,  $Pr = 1$  and  $Fr = 1$ . The dynamic Smagorinsky model is used as the SGS model. LES is run in low-res (Table 3) setting, after the accuracy of mixing is confirmed on the basis of convergence tests for the geom1 and geom2 settings. Mixing is calculated using the background potential energy method developed by Tseng and Ferziger (2001). We also tested briefly SAM in comparison to results from two-layer inviscid theory, which predicts the shape of the density interface in steady state flows, but not the mixing or the transient behavior. A good agreement is found between SAM and two-layer theory regarding the steady-state location of the density interface.

On the basis of the idealized experiments using LES, significant differences in the amount of mixing are found among the different domain geometries. In particular,  $\mathcal{S}$ -shaped channel geom7 is shown to lead to the highest (1.36-fold more than the reference case) level of mixing, possibly because of the additional shears caused by side to side sloshing due to the centrifugal force. Vertical and horizontal constrictions geom4–geom5 that are off set with respect to the location of the initial density interface also act to enhance the mixing by the trapping and breaking of the internal waves in between the obstacles. On the other hand, vertical and horizontal constrictions overlapping with the initial density interface geom2-geom3 restrain the rate of the exchange flow, reduce vertical shears and therefore mixing. The lowest mixing (some 1.74-fold less than the reference case) is encountered  $\nabla$ -shaped channel (geom6).

Counterparts of these experiments are conducted with SAM in a domain of  $16 \times 1$  in the horizontal and vertical directions, respectively, and using a specification of the domain width via the  $B$ -function. SAM experiments are run at two spatial resolutions; using 32,768 points (low-res) corresponding to a single streamwise slice of low-res LES, and also at a much higher resolution of 2,097,152 points (mid-res3, Table 4). By comparing the spanwise-averaged density perturbation fields from LES to those from SAM, it is found that SAM can simulate the density structure within

an rms error of 14% to 20% (Table 5). Successfully represent the net effect of lateral constrictions on the general shape of the interface reasonably well. But SAM tends to overestimate mixing when compared to LES, by some 1.38 to 1.97 times for mid-res3, and significantly more for low-res. This difference appears to be mainly due to the inability of the 2D dynamics to facilitate the break down of KH rollers into smaller scales because of the lack of vortex dynamics in the span-wise direction. The difference in the size of the stratified overturns between SAM and LES is clearly visible in the snapshots of the density perturbation fields. Also, the mixing appears to be resolution dependent so that computations that compare well with LES results (Fig. 4) do not provide a computational gain anymore (high-res SAM in Table 4 vs low-res LES in Table 3).

For the second stage of our study of modeling exchange flows, observational data from the Bosphorus Strait is employed to test SAM in a realistic application. One of the main challenges at this stage is to express the complex width data in the form of a  $B$ -function. The simulations from SAM with a simple closure appear to be excessively diffusive and noisy. The excess diffusion/mixing is likely to be related to the dynamical simplifications due to the 2D nature of the model, as discussed above, while the noise appears to correlate well with the  $B$  function. As such, further post-processing of the  $B$  function can possibly reduce the noise, but this avenue is not pursued here. However, it is of interest to find out whether the VLES closure can improve the solution. We show that SAM can benefit significantly from such comprehensive turbulence closures.

Overall, we conclude that exchange flows in narrow straits pose significant computational challenges due to the details of domain geometry and their impact on mixing and hydraulic effects. SAM with the VLES turbulence closure appears to be an attractive modeling tool to pursue dynamical problems such as the effects of wind forcing and variations in net transport on exchange flows, provided that high resolutions are used, and the modeler is aware of the potential of excessive mixing and challenges of mapping a 3D geometry into a 2D representation.

## Acknowledgements

Ilıcak and Özgökmen greatly appreciate the support of the National Science Foundation via grant OCE 0620661 under the Collaborative Mathematics and Geoscience program. Özsoy would like to thank the Office of Naval Research Visiting Scientist Programme and the Turkish Scientific and Technical Research Council for their support that made this collaboration possible. Part of this activity was supported under the project 105G029 of TUBITAK. The majority of the computations were carried out in the University of Miami's computing center (<http://ccs.miami.edu/hpc/>), and we would like to thank Nicholas Tsinoremas, Joel Zysman, Ashwanth Srinivasan and Zonghun Hu for their help. An important portion of the computations were completed on SystemX at Virginia Tech's advanced research computing center (<http://www.arc.vt.edu>). We thank our close collaborator Traian Iliescu for providing the time on this facility. We thank two anonymous reviewers for many constructive comments, which helped significantly improve the manuscript.

## References

- Adams, J., 1990. Mudpack: multigrid software for linear elliptic partial differential equations. SCD UserDoc, Version 2.0. NCAR.
- Andreassen, O., Hvidsten, P.O., Fritts, D.C., Arendt, S., 1998. Vorticity dynamics in a breaking internal gravity wave. Part 1. Initial instability evolution. *J. Fluid Mech.* 367, 27–46.
- Arakawa, A., 1966. Computational design for long-term numerical integration of the equations of fluid motion: two dimensional incompressible flow. Part i. *J. Comput. Phys.* 1, 119–143.
- Benjamin, T.B., 1968. Gravity currents and related phenomena. *J. Fluid Mech.* 31, 209–248.
- Bourgault, D., Kelley, D., 2004. A laterally averaged nonhydrostatic ocean model. *J. Atmos. Ocean. Technol.* 21, 1910–1924.
- Britter, R.E., Linden, P.F., 1980. The motion of the fronts of a gravity current traveling down an incline. *J. Fluid Mech.* 99, 531–543.
- Cantero, M.L., Lee, J.R., Balachandar, S., Garcia, M., 2007. On the front velocity of gravity currents. *J. Fluid Mech.* 586, 1–39.
- Chang, Y., Xu, X., Özgökmen, T., Chassignet, E., Peters, H., Fischer, P., 2005. Comparison of gravity current mixing parameterizations and calibration using a high-resolution 3d nonhydrostatic spectral element model. *Ocean Modell.* 10, 342–368.
- Corcos, G., Sherman, S., 1984. The mixing layer: deterministic models of a turbulent flow. Part 1. Introduction and the two-dimensional flow. *J. Fluid Mech.* 139, 29–65.
- Deville, M., Fischer, P., Mund, E., 2002. High-order methods for incompressible fluid flow, volume 9 of Cambridge Monographs on Applied and Computational Mathematics. Cambridge University Press, Cambridge, 2002. ISBN 0-521-45309-7.
- Dryja, M., Widlund, O.B. 1987. An additive variant of the Schwarz alternating method for the case of many subregions. Technical Report Technical Report 339, Dept. Computer Science, Courant Institute.
- Farmer, D.M., Armi, L., 1986. Maximal two-layer exchange over a sill and through the combination of a sill and contraction with barotropic flow. *J. Fluid Mech.* 164, 53–76.
- Fischer, P., Gottlieb, D., 1997. On the optimal number of subdomains for hyperbolic problems on parallel computers. *Int. J. Supercomput. Appl. High Perform. Comput.* 11, 65–76.
- Fischer, P.F., 1997. An overlapping Schwarz method for spectral element solution of the incompressible Navier-Stokes equations. *J. Comp. Physiol.* 133, 84–101.
- Fischer, P.F., Miller, N.I., Tufo, H.M., 2000. An overlapping Schwarz method for spectral element simulation of three-dimensional incompressible flows. In: Luskin, P.B.M. (Ed.), *Parallel Solution of Partial Differential Equations*. Springer-Verlag, pp. 159–181.
- Fischer, P.F., Ronquist, E.M., 1994. Spectral element methods for large scale parallel Navier-Stokes calculation. *Comput. Method. Appl. M.* 116, 69.
- Fritts, D.C., Arendt, S., Andreassen, O., 1998. Vorticity dynamics in a breaking internal gravity wave. Part 2. Vortex interactions and transition to turbulence. *J. Fluid Mech.* 367, 47–65.
- Germano, M., Piomelli, U., Moin, P., Cabot, W., 1991. A dynamic subgrid-scale eddy viscosity model. *Phys. Fluids A* 3, 1760–1765.
- Göktaşan, E., Tur, H., Ecevitoglu, B., Görüm, T., Türker, A., Tok, B., Çağlak, F., Birkan, H., Şimşek, M., 2005. Evidence and implications of massive erosion along the Strait of İstanbul (Bosphorus). *Geo-Mar. Lett.* 25, 324–342.
- Gregg, M.C., Özsoy, E., 1999. Mixing on the Black Sea shelf north of the Bosphorus. *Geophys. Res. Lett.* 26, 1869–1872.
- Gregg, M.C., Özsoy, E., 2002. Flow, water mass changes, and hydraulics in the Bosphorus. *J. Geophys. Res. (Oceans)* 107, 3016–+.
- Gregg, M.C., Özsoy, E., Latif, M.A., 1999. Quasi-steady exchange flow in the Bosphorus. *Geophys. Res. Lett.* 26, 83–86.
- Härtel, C., Meiburg, E., Necker, F., 2000. Analysis and direct numerical simulation of the flow at a gravity-current head. Part 1. Flow topology and front speed for slip and no-slip boundaries. *J. Fluid Mech.* 418, 189–212.
- Ilıcak, M., Özgökmen, T.M., Peters, H., Baumert, Z.H., Iskandarani, M., 2008. Very large eddy simulation of the red sea overflow. *Ocean Modell.* 20, 183–206.
- Iliescu, T., Fischer, P., 2003. Large eddy simulation of turbulent channel flows by the rational LES model. *Phys. Fluids* 15 (10), 3036–3047.
- Iliescu, T., Fischer, P., 2004. Backscatter in the rational LES model. *Comput. Fluids* 35 (5–6), 783–790.
- Kantha, L.H., Clayson, C.A., 1994. An improved mixed layer model for geophysical applications. *J. Geophys. Res.* 99, 25235–25266.
- Klaassen, G.P., Peltier, W.R., 1989. The role of transverse secondary instabilities in the evolution of free shear layers. *J. Fluid Mech.* 202, 367–402.
- Klaassen, G.P., Peltier, W.R., 1991. The influence of stratification on secondary instability in free shear layers. *J. Fluid Mech.* 227, 71–106.
- Latif, M.A., Özsoy, E., Oğuz, T., Ünlüata, Ü., 1991. Observations of the Mediterranean inflow into the Black Sea. *Deep Sea Res.* 38 (Suppl. 2), S711–S723.
- Lottes, J.W., Fischer, P.F., 2005. Hybrid multigrid/Schwarz algorithms for the spectral element method. *J. Sci. Comput.* 24 (1), 45–78.
- Maday, Y., Patera, A.T., 1989. Spectral element methods for the Navier-Stokes equations. In: Noor, A.K. (Ed.), *State of the Art Surveys in Computational Mechanics*. ASME, pp. 71–143.
- Maday, Y., Patera, A.T., Rønquist, E.M., 1990. An operator-integration-factor splitting method for time-dependent problems: application to incompressible fluid flow. *J. Sci. Comput.* 10, 496–508.
- Magagnato, F., Gabi, M., 2002. A new turbulence model for unsteady flow fields in rotating machinery. *Int. J. Rot. Machinery* 8 (3), 175–183.
- Mason, P.J., 1989. Large-eddy simulation of the convective atmospheric boundary layer. *J. Atmos. Sci.* 46, 1492–1516.
- Mason, P.J., Thomson, D.J., 1992. Stochastic backscatter in large-eddy simulations of boundary layers. *J. Fluid Mech.* 242, 51–78.
- Meneveau, C., Lund, T., Cabot, W., 1996. A Lagrangian dynamic subgrid-scale model of turbulence. *J. Fluid Mech.* 319, 353–385.
- Monaghan, J.J., 2007. Gravity current interaction with interfaces. *Ann. Rev. Fluid Mech.* 39, 245–261.

- Oğuz, T., 2005. Hydraulic adjustments of the Bosphorus exchange flow. *Geophys. Res. Lett.* 32, L06604.
- Oğuz, T., Özsoy, E., Latif, M.A., Sur, H.I., Ünlüata, Ü., 1990. Modeling of hydraulically controlled exchange flow in the Bosphorus Strait. *J. Phys. Oceanogr.* 20, 945–965.
- Oğuz, T., Sur, H.I., 1989. A two-layer model of the water exchange through the Dardanelles Strait. *Oceanol. Acta* 12, 23–31.
- Özgökmen, T., Fischer, P., 2008. On the role of bottom roughness in overflows. *Ocean Modell.* 20, 336–361.
- Özgökmen, T., Iliescu, T., Fischer, P., 2009. Large eddy simulation of stratified mixing in a three-dimensional lock-exchange system. *Ocean Modell.* 26, 134–155.
- Özgökmen, T.M., Fischer, P.F., Duan, J., Iliescu, T., 2004a. Entrainment in bottom gravity currents over complex topography from three-dimensional nonhydrostatic simulations. *Geophys. Res. Lett.* 31, L13212.
- Özgökmen, T.M., Fischer, P.F., Duan, J., Iliescu, T., 2004b. Three-dimensional turbulent bottom density currents from a high-order nonhydrostatic spectral element model. *J. Phys. Oceanogr.* 34.
- Özgökmen, T.M., Fischer, P.F., Johns, W.E., 2006. Product water mass formation by turbulent density currents from a high-order nonhydrostatic spectral element model. *Ocean Modell.* 12, 237–267.
- Özgökmen, T.M., Iliescu, T., Fischer, P.F., Srinivasan, A., Duan, J., 2007. Large eddy simulation of stratified mixing in two-dimensional dam-break problem in a rectangular enclosed domain. *Ocean Modell.* 16, 106–140.
- Özsoy, E., Di Iorio, D., Gregg, M., Backhaus, J., 2001. Mixing in the Bosphorus Strait and the Black Sea continental shelf: observations and a model of the dense water outflow. *J. Marine Syst.* 31, 99–135.
- Özsoy, E., Latif, M.A., Beşiktepe, Ş., Çetin, N., Gregg, N., Belokopytov, V., Goryachkin, Y., Diaconu, V., 1998. The Bosphorus Strait: exchange fluxes, currents and sea-level changes. In Ivanov, L.I. and T. Oguz, editors, *The Bosphorus Strait: exchange fluxes, currents and sea-level changes*, NATO Science Series 2: Environmental Security, {47}, pages vol.1, 367pp+vol. 2, 385pp. Kluwer Academic Publishers, Dordrecht.
- Özsoy, E., Latif, M.A., Beşiktepe, Ş., Gaines, A.F., 1995a. Fluorescent dye measurements of the mixing and transport of wastewater discharge in the Bosphorus. *Wat. Sci. Tech.* 32, 61–68.
- Özsoy, E., Latif, M.A., Sur, H.I., Goryachkin, Y., 1996. A review of the exchange flow regimes and mixing in Bosphorus Strait. In: Briand, F. (Ed.), *Bulletin de l'Institut Océanographique. Mediterranean Tributary Seas*, Monaco.
- Özsoy, E., Latif, M.A., Tuğrul, S., Ünlüata, Ü., 1995b. Exchanges with the Mediterranean, fluxes and boundary mixing processes in the Black Sea. In: Briand, F. (Ed.), *Bulletin de l'Institut Océanographique. Mediterranean Tributary Seas*, Monaco, pp. 1–25.
- Özsoy, E., Ünlüata, Ü., 1997. Oceanography of the Black Sea: a review of some recent results. *Earth Sci. Rev.* 42, 231–272.
- Özsoy, E., Ünlüata, Ü., 1998. The Black Sea. In: Robinson, A.R., Brink, K. (Eds.), *The Sea The Global Coastal Ocean: Regional Studies and Syntheses*, vol. 11. John Wiley and Sons, pp. 889–914.
- Patera, A., 1984. A spectral element method for fluid dynamics; laminar flow in a channel expansion. *J. Comp. Phys.* 54, 468–488.
- Polat, Ç., Tuğrul, S., 1995. Nutrient and organic carbon exchanges between the Black and Marmara Seas through the Bosphorus Strait. *Cont. Shelf Res.* 15, 1115–1132.
- Porté-Agel, F., Meneveau, C., Parlange, M.B., 2000. A scale-dependent dynamic model for large-eddy simulation: application to a neutral atmospheric boundary layer. *J. Fluid Mech.*, 415:261–284. ISSN 0022-1120.
- Ruprecht, A., Helmrigh, T., Buntić, I., 2003. Conference on modelling fluid flow (cmff03). In: *The 12th International Conference on Fluid Flow Technologies*, Budapest, Hungary.
- Simpson, J.E., 1987. *Gravity Currents in the Environment and the Laboratory*. John Wiley and Sons.
- Tseng, Y., Ferziger, J., 2001. Mixing and available potential energy in stratified flows. *Phys. Fluids* 13, 1281–1293.
- Tufo, H.M., Fischer, P., 2001. Fast parallel direct solvers for coarse grid problems. *J. Parallel Distr. Comput.* 173, 431–471.
- Ünlüata, Ü., Oğuz, T., Latif, M.A., Özsoy, E., 1990. On the physical oceanography of the Turkish Straits. In: Pratt, L.J. (Ed.), *The Physical Oceanography of Sea Straits*, NATO/ASI Series, Kluwer, Dordrecht, pp. 26–60.
- Van Driest, E.R., 1956. On turbulent flow near a wall. *J. Aerospace Sci.* 23, 1007–1011.
- Winters, K.B., Lombard, P.N., Riley, J.J., D'Asaro, E.A., 1995. Available potential energy and mixing in density-stratified fluids. *J. Fluid Mech.* 289, 115–128.
- Winters, K.B., Seim, H.E., 2000. The role of dissipation and mixing in exchange flow through a contracting channel. *J. Fluid Mech.* 407, 265–290.
- Xu, X., Chang, Y., Peters, H., Özgökmen, T., Chassignet, E., 2006. Parameterization of gravity current entrainment for ocean circulation models using a high-order 3d nonhydrostatic spectral element model. *Ocean Modell.* 14, 19–44.
- Zalesak, S.T., 1978. Fully multidimensional flux-corrected transport algorithms for fluids. *J. Comput. Phys.* 31, 335–362.